SIAM J. IMAGING SCIENCES
Vol. 5, No. 1, pp. 311–342
© 2012 Society for Industrial and Applied Mathematics

Perspective Shape from Shading: Ambiguity Analysis and Numerical Approximations*

Michael Breuß†, Emiliano Cristiani‡, Jean-Denis Durou§, Maurizio Falcone¶, and Oliver Vogel†

Abstract. In this paper we study a perspective model for shape from shading and its numerical approximation. We show that an ambiguity still persists, although the model with light attenuation factor has previously been shown to be well-posed under appropriate assumptions. Analytical results revealing the ambiguity are complemented by various numerical tests. Moreover, we present convergence results for two iterative approximation schemes. The first is based on a finite difference discretization, whereas the second is based on a semi-Lagrangian discretization. The convergence results are obtained in the general framework of viscosity solutions of the underlying partial differential equation. In addition to these theoretical and numerical results, we propose an algorithm for reconstructing discontinuous surfaces, making it possible to obtain results of reasonable quality even for complex scenes. To this end, we solve the constituting equation on a previously segmented input image, using state constraint boundary conditions at the segment borders.

Key words. shape from shading, ambiguity analysis, Hamilton–Jacobi equations, finite difference methods, semi-Lagrangian schemes

AMS subject classifications. 68U10, 35A02, 65N06, 65N12, 65N20, 65N21

DOI. 10.1137/100815104

1. Introduction.

The shape from shading (SFS) problem amounts to the reconstruction of the three-dimensional (3-D) structure of objects given a single two-dimensional (2-D) gray value image of them. For this task, the SFS process relies on information on the illumination and the light reflectance in the scene. It was introduced by Horn [20] and is a classic inverse problem in computer vision with many potential applications; see, e.g., [16, 21, 22, 38] and the references therein for an overview.

In this paper we deal with a perspective SFS model as proposed in [25, 31, 34], taking into account the so-called light attenuation factor; cf. [31]. This SFS model has gained some attention in the recent literature. It combines desirable theoretical properties with a reasonable quality of results compared to other approaches in SFS. One of its good theoretical properties

*Received by the editors November 16, 2010; accepted for publication (in revised form) November 26, 2011; published electronically March 8, 2012. This work was partially supported by the PRIN 2007 Project "Metodologie per il calcolo scientifico ed applicazioni avanzate" and by the Deutsche Forschungsgemeinschaft (DFG).
http://www.siam.org/journals/siims/5-1/81510.html

†Faculty of Mathematics and Computer Science, Saarland University, Building E1.1, 66041 Saarbrücken, Germany (breuss@mia.uni-saarland.de, vogel@mia.uni-saarland.de).

‡Dipartimento di Matematica, SAPIENZA Università di Roma, P.le Aldo Moro 2, 00185 Rome, Italy (e.cristiani@iac.cnr.it).

§Institut de Recherche en Informatique de Toulouse, Université Paul Sabatier, 118 route de Narbonne, 31062 Toulouse Cédex 9, France, and Centre de Mathématiques et de Leurs Applications, École Normale Supérieure de Cachan, 61 avenue du président Wilson, 94235 Cachan Cédex, France (durou@irit.fr).

¶Corresponding author. Dipartimento di Matematica, SAPIENZA Università di Roma, P.le Aldo Moro 2, 00185 Rome, Italy (falcone@mat.uniroma1.it).

is the well-posedness, given some assumptions. However, the question arises whether all the ambiguities (including the notorious concave/convex ambiguity [20]) have been entirely vanquished by using the perspective SFS model. For the case that the answer is negative, it would be of interest to determine whether there is a way to avoid ambiguities. Concerning the numerical realization of the model, a number of iterative solvers have been proposed and compared [6]. However, the mathematical validation of some of them is still lacking.

In this paper we address these open issues. By a thorough investigation, we show that ambiguities still arise and appear in practical computations. We propose a way of overcoming those ambiguities whenever they are caused only by the discontinuity of the surface to be reconstructed. We do this by making use of a segmentation step combined with suitable boundary conditions at the segment borders. In this way, shapes in relatively complex scenes also can be reconstructed. Moreover, we prove that the two fastest and easiest-to-implement iterative solvers selected in the comparative paper [6] converge to the viscosity solution of the considered equation.

Models and ambiguities. Perspective SFS models are distinguished by the assumption that the camera performs a perspective projection of the 3-D world to the given 2-D image. Recently, a number of perspective SFS models have been considered [11, 29, 34], with promising applications to face reconstruction [29], reconstruction of organs [34, 35], and digitization of documents [11, 12].

Within the class of perspective SFS models, that of Okatani and Deguchi [25] is distinguished by the lighting model. This consists of a point light source located at the optical center combined with a light attenuation term. Okatani and Deguchi proposed a method for resolving their model which is an extension of the level set method designed by Kimmel et al. [23] for solving the classic SFS problem. They claimed that their method could be derived from a partial differential equation (PDE) of the form $H(x, y, r, r_x, r_y) = 0$, where r is the distance to the point light source, but did not explicitly state it. Prados, Faugeras, and Camilli stated in [32] the first PDE derived from this model, which we now call the *PSFS model* ("P" for "perspective"). A number of papers by Prados and his coauthors have dealt with its theoretical basis; cf. [27, 28, 30, 31]. Especially, the PSFS model has been shown to be well-posed under mild assumptions.

The well-posedness of SFS models has been a point of continuous interest in computer vision research. This began with Horn [20] who mentions the concave/convex ambiguity in his classic orthographic SFS model; see [22] for extensive discussion. Two main features for proofs of existence and uniqueness of the solution are the singular points (which are the points where the surface faces the light) and the limbs (where the light rays graze the surface, sometimes also referred to as horizons, motivated by the optimal control formulation of the problem) [4, 7, 8, 17, 26], since the surface normal in such points can be computed without ambiguity.

It turns out that the classic concave/convex ambiguity is not the only source of nonuniqueness. Starting from a paper by Rouy and Tourin [33], a modern tool for understanding the hyperbolic PDEs that arise in SFS is the notion of viscosity solutions. For the classic SFS model investigated in [33], one can see that there are still several weak solutions in the viscosity sense whenever there exist points at maximum brightness (i.e., $I = 1$) in the image. These points are called *singular points*. This lack of uniqueness is a fundamental property of the underlying class of PDEs. In order to achieve uniqueness in this setting, one may add informa-

tion such as the height at each singular point [24], one may characterize the so-called maximal solution [9, 19], or one may employ a combination of these approaches [27, 28]. However, we note that the framework of viscosity solutions for these types of equations is very natural and is mainly motivated by stability properties, which guarantee that viscosity solutions can be obtained in the limit by adding a regularization term to the first order equation (typically, a second order term) and letting this term go to 0. We refer the interested reader to the classic book by Barles [1] for the properties of viscosity solutions and to [10] for their use in image processing problems. Let us also mention that a discussion on instabilities arising in the solution of the Eikonal equation for the SFS problem is presented in [3].

Numerical methods for PSFS. A number of recent papers have considered the numerical implementation of the PSFS model. The original scheme of Prados and colleagues (see especially [31]) relies on the optimal control formulation of the PSFS model. It solves the underlying Hamilton–Jacobi–Bellman equation using a top-down dynamic programming approach. However, the method is difficult to implement as it relies on the analytical solution of an incorporated optimization problem involving many distinct cases. In [14] a semi-Lagrangian method, indicated by CFS, has been proposed. This method also relies on the Hamilton–Jacobi–Bellman equation, but it is easier to code. An alternative approach has been explored in [37], where the Hamilton–Jacobi equation corresponding to the PSFS model has been discretized by a finite difference scheme, indicated by VBW. All the schemes mentioned as well as their algorithmic extensions have been studied experimentally in [6]. According to the results presented there, the latter two schemes, i.e., CFS and VBW, have been identified as the most efficient methods with respect to run times and implementation effort.

Our contribution. The novelties of this paper can be summarized as follows.

(i) We explain in detail why the PSFS model cannot be considered completely well-posed as concluded in [31, 32]. To this end, we show analytically that *ambiguities still exist*, and we present numerical computations proving the practical importance of these ambiguities.

(ii) We prove convergence to the viscosity solution of both the CFS [14] and the VBW [37] schemes. For validating the convergence of the latter, we show how to make use of previous work by Barles and Souganidis [2]. Concerning the proof of convergence for the CFS scheme, we do not rely on that classic approach. Our proof relies on the idea that the CFS iterates are monotone decreasing (in the sense of pointwise comparison) as well as bounded from below, implying convergence. A similar strategy has been used in [5] in the context of hyperbolic conservation laws.

(iii) Relying on the results from (i) and (ii), we explore an algorithmic way of computing reasonable solutions if the surface to be reconstructed is discontinuous. This is done via a presegmentation of the input image which allows us to detect and isolate continuous parts of the PSFS solution. Segment borders are precisely the points where the considered numerical schemes strive for a viscous approximation of a continuous solution and where ambiguities may arise. In these points, state constraint boundary conditions are employed. We show experimentally that our set-up gives reasonable results using synthetic and real-world data.

Paper organization. The paper is organized as follows. In section 2, we briefly review the model and related equations. The ambiguity problem is discussed in detail in section 3. The numerical methods and their convergence are considered in section 4. In section 5 we deal with discontinuous surfaces, describing an algorithm which couples a segmentation technique and

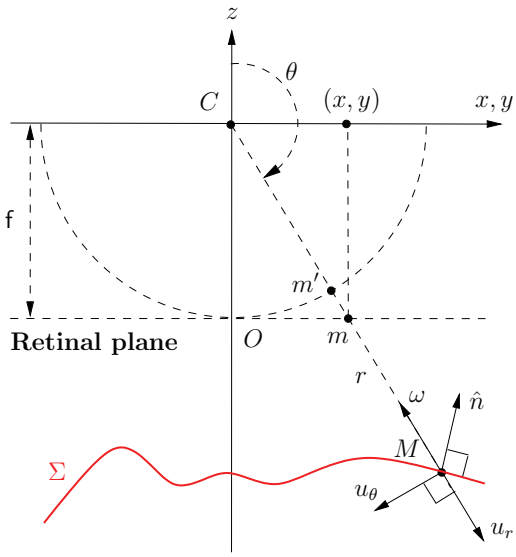

Figure 1. *Notation for the PSFS model with point light source at the optical center.*

the PSFS equation. The paper ends with a conclusion. Some technical issues are described in two appendices.

2. The PSFS model and related equations. In this section, we recall, for the reader's convenience, the model for PSFS with a point light source located at the optical center and a light attenuation term. We also recall the first related PDE associated to the model, derived in [32].

2.1. The PSFS model with light attenuation. Let (x, y) be a point in the image domain Ω, where Ω is an open bounded subset of $\mathbb{R}^2$. Furthermore, let

- $I = I(x, y) > 0$ be the normalized brightness function. We have $I = \frac{E(x,y)}{\sigma}$, where E is the gray level of the given image and σ is the product of the surface albedo (which tells us to which extent the surface reflects light) and the light source intensity;
- f be the focal length, i.e., the distance between the optical center C of the camera and the 2-D plane to which the scene of interest is mapped (see Figure 1).

Let M be a generic point on the surface Σ to be reconstructed. We choose as the unknown of the problem the function $u : \Omega \to \mathbb{R}$ such that

$$M = M(x, y) = u(x, y)\, m' \,, \tag{2.1}$$

where

$$m' = \frac{\mathsf{f}}{\sqrt{x^2 + y^2 + \mathsf{f}^2}}\, m \quad \text{and} \quad m = (x, y, -\mathsf{f})^\top. \tag{2.2}$$

Another definition of the unknown u is given by the relation $M(x, y) = u(x, y)\, m$, which differs from (2.1) and leads to a slightly different PDE, as shown in [32].

Note that, according to this notation, $u > 0$ holds as the depicted scene is in front of the camera. We denote by $r(x, y)$ the distance between the point light source and the point $M(x, y)$ on the surface. It holds that $u(x, y) = r(x, y)/\mathsf{f}$, since the light source location coincides with the optical center.

The model associated to the PSFS problem is obtained by the *image irradiance equation*,

$$R(\widehat{n}(x, y)) = I(x, y), \tag{2.3}$$

making explicit the unit normal $\widehat{n}$ to the surface and the reflectance function R which gives the value of the light reflection on the surface as a function of its normal.

We denote by $\omega(x, y)$ the unit vector representing the light source direction at the point $M(x, y)$ (note that in the classic SFS model this vector is constant):

$$\omega(x, y) = \frac{(-x, -y, \mathsf{f})^\top}{\sqrt{x^2 + y^2 + \mathsf{f}^2}}. \tag{2.4}$$

Adding the assumptions of a *light attenuation term* and of a *Lambertian surface*, the function R is defined as

$$R(\widehat{n}(x, y)) = \frac{\omega(x, y) \cdot \widehat{n}(x, y)}{r(x, y)^2}, \tag{2.5}$$

with an attenuation factor which is equal to the inverse of the squared distance from the source. Expression (2.5) would still hold for any location of the point light source, but the same would not be true for the equality $u(x, y) = r(x, y)/\mathsf{f}$ or for (2.4). The case of a light source coinciding with the optical center corresponds more or less to endoscopic images [25] and to photographs taken at short distances with the camera flash [32]. Another considerable advantage of the PSFS model using a point light source at the optical center is that there is no shadow in the image.

Finally, by (2.3) and (2.5) we obtain the PSFS equation

$$\frac{\omega(x, y) \cdot \widehat{n}(x, y)}{r(x, y)^2} = I(x, y). \tag{2.6}$$

2.2. The corresponding Hamilton–Jacobi equation. In order to write the corresponding PDE, it is useful to introduce the new unknown $v = \ln(u)$ (we recall that $u > 0$). Equation (2.6) can be written as a static Hamilton–Jacobi equation (see [31, 32] and Appendix A for details),

$$H(x, y, v, \nabla v) := \frac{I(x, y)}{Q(x, y)} \mathsf{f}^2 W(x, y, \nabla v) - e^{-2v(x,y)} = 0, \quad (x, y) \in \Omega, \tag{2.7}$$

where

$$Q(x, y) := \frac{\mathsf{f}}{\sqrt{x^2 + y^2 + \mathsf{f}^2}} \tag{2.8}$$

(which is equal to $|\cos\theta|$; cf. Figure 1) and

$$W(x, y, \nabla v) := \sqrt{\mathsf{f}^2 \|\nabla v\|^2 + (\nabla v \cdot (x, y))^2 + Q(x, y)^2} \tag{2.9}$$

($\|\cdot\|$ denotes the Euclidean norm). Note that $W(x,y,\nabla v)$ is convex with respect to $\nabla v \in \mathbb{R}^2$, and then the same property holds for the Hamiltonian H.

The existence and uniqueness of the viscosity solution of (2.7) is proved in [32]. In the same paper some possible choices for the boundary conditions are discussed.

Equation (2.7) also admits a "control formulation" which can be helpful. In [32] it is shown that v is the solution of the following Hamilton–Jacobi–Bellman-like equation:

$$-e^{-2v(x,y)} + \sup_{a\in\overline{B(0,1)}} \{-b(x,y,a)\cdot\nabla v(x,y) - \ell(x,y,a)\} = 0, \tag{2.10}$$

where $\overline{B(0,1)}$ denotes the closed unit ball in $\mathbb{R}^2$ and the other terms in (2.10) are defined as follows:

$$\ell(x,y,a) := -I(x,y)\,\mathsf{f}^2\sqrt{1-\|a\|^2}\,, \qquad b(x,y,a) := -JG^TDGa\,, \tag{2.11}$$

with

$$J(x,y) := \frac{I(x,y)}{Q(x,y)}\mathsf{f}^2 = I(x,y)\mathsf{f}\sqrt{\mathsf{f}^2+x^2+y^2}\,, \tag{2.12}$$

$$G(x,y) := \begin{cases} \frac{1}{\sqrt{x^2+y^2}}\begin{pmatrix} y & -x \\ x & y\end{pmatrix} & \text{if } (x,y)\neq(0,0), \\ \begin{pmatrix} 1 & 0 \\ 0 & 1\end{pmatrix} & \text{if } (x,y)=(0,0), \end{cases} \tag{2.13}$$

$$D(x,y) := \begin{pmatrix} \mathsf{f} & 0 \\ 0 & \sqrt{\mathsf{f}^2+x^2+y^2}\end{pmatrix}. \tag{2.14}$$

3. Ambiguities.

In this section we show that the model presented above suffers from an ambiguity which shares some features with the classic concave/convex ambiguity. We also show in detail in which case it is numerically possible to reconstruct the expected surface and in which case a different surface is computed.

3.1. The ambiguity in the model.

In order to prove the existence of two different surfaces associated to the same brightness function I, it is convenient to reformulate the problem in standard spherical coordinates (r,θ,ϕ): the parameters of an image point $m(\theta,\phi)$ are now the angles θ and ϕ, which are, respectively, the colatitude and the longitude of the conjugated object point $M(\theta,\phi)$, with respect to the camera coordinate system $(Cxyz)$. Let us note that only the object points $M(\theta,\phi)$ such that $\theta\in]\pi/2,\pi]$ are visible (see Figure 1), whereas $\phi\in[0,2\pi[$. Given a brightness function $I(\theta,\phi)$, we are looking for a surface Σ in the form $r=r(\theta,\phi)$ such that

$$\frac{\omega(\theta,\phi)\cdot\widehat{n}(\theta,\phi)}{r(\theta,\phi)^2} = I(\theta,\phi). \tag{3.1}$$

A generic point M has coordinates

$$M(\theta,\phi) = \begin{pmatrix} r(\theta,\phi)\sin\theta\cos\phi \\ r(\theta,\phi)\sin\theta\sin\phi \\ r(\theta,\phi)\cos\theta \end{pmatrix}_{(Cxyz)} \tag{3.2}$$

with respect to the coordinate system $(Cxyz)$. We now introduce the local orthonormal basis $\mathcal{S} = (u_r, u_\theta, u_\phi)$ of $\mathbb{R}^3$ defined by

$$u_r := \frac{M(\theta,\phi)}{r(\theta,\phi)}, \qquad u_\theta := \frac{\partial_\theta u_r}{\|\partial_\theta u_r\|}, \qquad \text{and} \qquad u_\phi := \frac{\partial_\phi u_r}{\|\partial_\phi u_r\|}, \tag{3.3}$$

which depends on the point M (see Figure 1). The expression of $\widehat{n}$ in this new basis is (see Appendix B for details)

$$\widehat{n}(\theta,\phi) = \frac{1}{((r^2 + {r_\theta}^2)\sin^2\theta + {r_\phi}^2)^{1/2}} \begin{pmatrix} -r\sin\theta \\ r_\theta \sin\theta \\ r_\phi \end{pmatrix}_{\mathcal{S}}, \tag{3.4}$$

where the dependence of r, r_θ, and r_ϕ on (θ,ϕ) is omitted. Using (3.4) and considering that ω coincides with $-u_r$ (since the point light source is located at the optical center), (3.1) can be rewritten as

$$r^2\left(r^2 + {r_\theta}^2 + \frac{{r_\phi}^2}{\sin^2\theta}\right) = \frac{1}{I^2}. \tag{3.5}$$

We now return to our purpose. We choose as reference surface $\overline{\Sigma}$ the hemisphere $r(\theta,\phi) \equiv 1$, where $(\theta,\phi) \in]\pi/2,\pi] \times [0,2\pi[$, which is associated to the brightness function $I_{\overline{\Sigma}}(\theta,\phi) \equiv 1$ (see Figure 2).

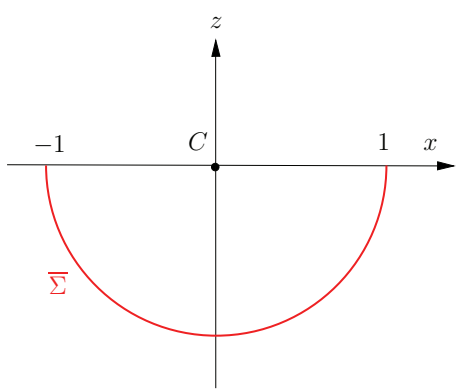

Figure 2. *Hemisphere $\overline{\Sigma}$: Do other surfaces give the same brightness function $I_{\overline{\Sigma}} \equiv 1$?*

Then, we look for other surfaces which are not isometric to $\overline{\Sigma}$ but give the same brightness function. For the sake of simplicity, let us limit our search to the surfaces which are circularly symmetric around the optical axis Cz, i.e., to the functions r of the form $r(\theta,\phi) = r(\theta)$. Equation (3.5) is thus simplified to the ordinary differential equation

$$r^2(r^2 + {r_\theta}^2) = \frac{1}{{I_{\overline{\Sigma}}}^2} = 1, \tag{3.6}$$

which can be rewritten as

$$\frac{r\,dr}{\sqrt{1-r^4}} = \pm d\theta \tag{3.7}$$

since (3.6) imposes $r \leq 1$. Integrating (3.7), we obtain the following solutions depending on a parameter θ_0, which is a constant of integration:

$$r_{\theta_0}(\theta) = \sqrt{\cos(2(\theta - \theta_0))}. \tag{3.8}$$

Surfaces Σ. Let us denote as Σ_{θ_0} the surface of the equation $r = r_{\theta_0}(\theta)$. Note that (3.8) imposes that $\theta \in]\theta_0 - \pi/4, \theta_0 + \pi/4[$ (bounds excluded because $r > 0$). Since $\theta \in]\pi/2, \pi]$ by definition, each surface Σ_{θ_0} has the same brightness $I \equiv 1$ as $\overline{\Sigma}$ in a part $\mathcal{D}_{\theta_0}$ of the image plane, i.e., in its domain of definition, which is circularly symmetric around the optical axis Cz and contains the points such that $\theta \in \mathcal{I}_{\theta_0} =]\theta_0 - \pi/4, \theta_0 + \pi/4[\cap]\pi/2, \pi]$. If we require $\mathcal{D}_{\theta_0}$ to be nonempty and to contain $\theta = \pi$, i.e., the origin O in the image plane, this implies that the parameter θ_0 in (3.8) is in the interval $]3\pi/4, 5\pi/4[$. Then, we see that $\mathcal{I}_{\theta_0} =]\theta_0 - \pi/4, \pi]$ and that $\mathcal{D}_{\theta_0}$ is a disc of center O and of radius $\rho_{\theta_0} = \mathsf{f} \tan(5\pi/4 - \theta_0)$.

Since all the surfaces Σ_{θ_0}, for $\theta_0 \in]3\pi/4, 5\pi/4[$, are circularly symmetric around the optical axis Cz, we can simplify the 3-D setting of spherical coordinates to two dimensions, omitting the angle describing the location of points with respect to the y-axis. Doing so, we have represented the four surfaces Σ_{θ_0} which correspond to $\theta_0 = 3\pi/4^+$, $\theta_0 = 7\pi/8$, $\theta_0 = \pi$, and $\theta_0 = 9\pi/8$ (cf. Figure 3). Note that among those surfaces, only Σ_π is differentiable everywhere (see Figure 3(c)). We thus have found two differentiable surfaces $\overline{\Sigma}$ and Σ_π which give exactly the same image in the disc $\mathcal{D}_\pi = (O, \mathsf{f})$ under the PSFS model with point light source at the optical center and light attenuation term.

It is important to stress that all other surfaces Σ_{θ_0}, for $\theta_0 \in]3\pi/4, \pi[\cup]\pi, 5\pi/4[$, have a unique singularity at their intersection with the optical axis (see Figures 3(a), 3(b), and 3(d)).

Surfaces Σ' and Σ''. Each surface Σ_{θ_0}, for $\theta_0 \in]3\pi/4, \pi[$, is tangent to the reference surface $\overline{\Sigma}$ in $\theta = \theta_0$. Therefore, other differentiable solutions, which are not of class C^2 but of class C^1, can be constructed by joining the differentiable part of Σ_{θ_0}, for $\theta_0 \in]3\pi/4, \pi[$, to $\overline{\Sigma}$. Two examples of such surfaces, which are denoted by Σ'_{θ_0}, are shown in Figures 4(a) and 4(b). Of course, the nondifferentiable part of Σ_{θ_0}, for $\theta_0 \in]3\pi/4, \pi[$, can also be joined to $\overline{\Sigma}$. These last solutions are denoted by Σ''_{θ_0} (see Figures 4(c) and 4(d)). The domains of definition of Σ'_{θ_0} and Σ''_{θ_0} are bounded by discs of center O and of radii $\rho'_{\theta_0} = \rho_{\theta_0} = \mathsf{f} \tan(5\pi/4 - \theta_0)$ and $\rho''_{\theta_0} = +\infty$, respectively.

To conclude, we have found four families of continuous surfaces which give the same image as $\overline{\Sigma}$, namely, $\{\Sigma_{\theta_0}\}_{\theta_0 \in]3\pi/4, \pi[}$, $\{\Sigma_{\theta_0}\}_{\theta_0 \in]\pi, 5\pi/4[}$, $\{\Sigma'_{\theta_0}\}_{\theta_0 \in]3\pi/4, \pi[}$, and $\{\Sigma''_{\theta_0}\}_{\theta_0 \in]3\pi/4, \pi[}$. In the next subsection, we will see that $\overline{\Sigma}$, which constitutes a common supersolution of all these solutions, is the initial surface used in the algorithm of Prados, Faugeras, and Camilli [32]. Let us also note that the surfaces $\{\Sigma'_{\theta_0}\}_{\theta_0 \in]3\pi/4, \pi[}$ are differentiable everywhere, and that $\Sigma'_{3\pi/4^+}$ (see Figure 4(a)) is of particular interest since it has the same domain of definition as $\overline{\Sigma}$. Let us finally note that there could exist further solutions which are not circularly symmetric around the optical axis.

The existence of many different surfaces having the same image does not contradict the uniqueness result proved in [31], since they correspond to different boundary conditions, or to the same boundary conditions imposed in a different domain of definition. We will see in the next subsection that all of these solutions can be computed by solving the PSFS equation (2.7), imposing appropriate boundary conditions on the appropriate domain. However, the

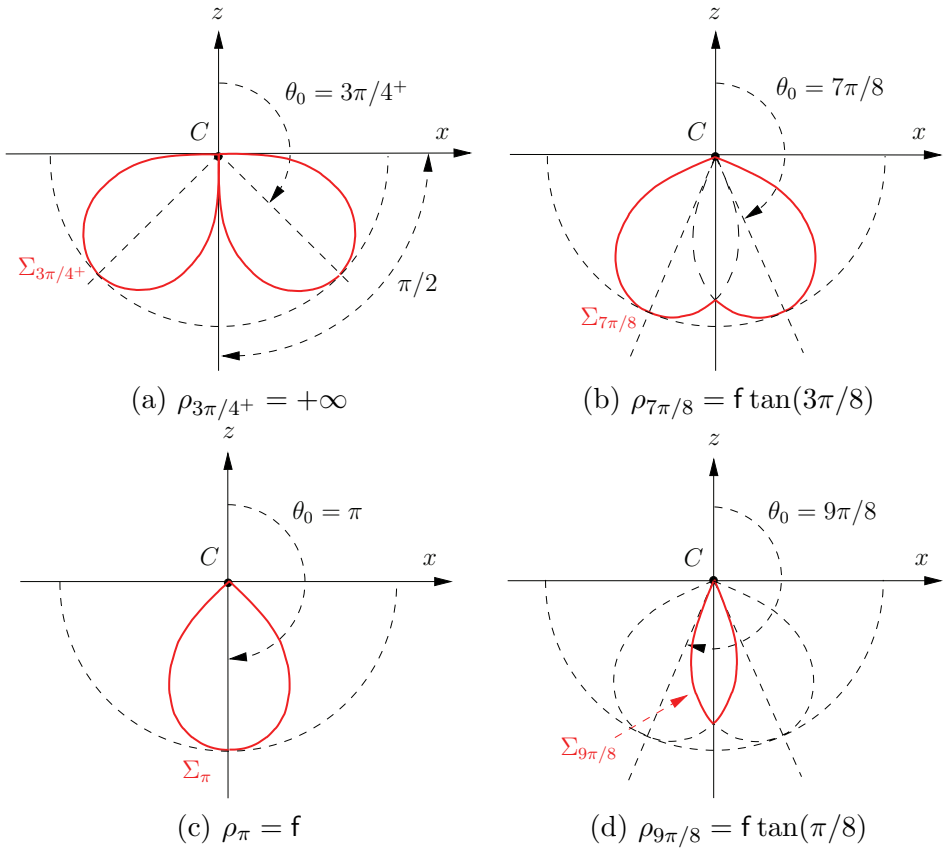

Figure 3. *The four surfaces $\Sigma_{3\pi/4^+}$, $\Sigma_{7\pi/8}$, Σ_π, and $\Sigma_{9\pi/8}$ drawn in red, which are circularly symmetric around the optical axis Cz, have the same image with uniform gray level $I \equiv 1$ as the hemisphere $\overline{\Sigma}$ shown in Figure 2, according to the PSFS model. They belong to the continuous family $\{\Sigma_{\theta_0}\}_{\theta_0 \in]3\pi/4, 5\pi/4[}$.*

counterexample exhibited in this subsection suffices to prove that the PSFS model is still ambiguous, even if only the surfaces defined on the whole image plane are considered: apart from $\overline{\Sigma}$, $\Sigma'_{3\pi/4^+}$ is differentiable everywhere, whereas all the surfaces Σ''_{θ_0}, for $\theta_0 \in]3\pi/4, \pi[$, are other weak solutions of the same problem.

3.2. Viscosity and weak solutions. In this subsection we investigate when the ambiguity arises solving the PSFS equation (2.7). The uniqueness of the viscosity solution of (2.7) was proved in [32] (see also [30]). Nevertheless, the uniqueness of the viscosity solution does not solve the problem of the model ambiguity, because we could be interested in the reconstruction of a surface described not by the viscosity solution but rather by another weak solution. This is a well-known issue in orthographic SFS with light beam parallel to the optical axis. Let us consider the simple case of a one-dimensional (1-D) gray level image with constant brightness function $I(x) \equiv \sqrt{2}/2$, and let us solve the SFS problem by means of the Eikonal equation

$$|z'(x)| = \sqrt{\frac{1}{I^2(x)} - 1}\,, \qquad x \in [-1, 1], \tag{3.9}$$

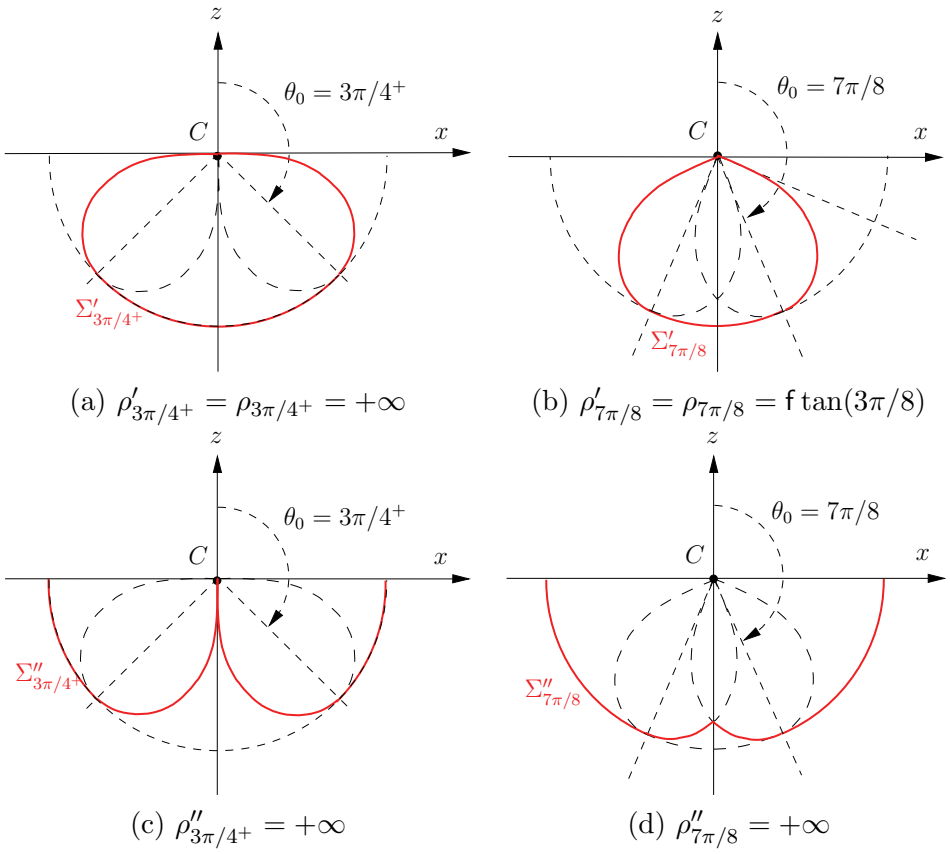

Figure 4. *The four surfaces drawn in red have the same image as $\overline{\Sigma}$, according to the PSFS model.* (a), (c) *The surfaces $\Sigma'_{3\pi/4^+}$ and $\Sigma''_{3\pi/4^+}$ are constructed by joining $\Sigma_{3\pi/4^+}$ (cf. Figure 3(a)) to $\overline{\Sigma}$ in two different ways.* (b), (d) *The surfaces $\Sigma'_{7\pi/8}$ and $\Sigma''_{7\pi/8}$ are constructed by joining $\Sigma_{7\pi/8}$ (cf. Figure 3(b)) to $\overline{\Sigma}$.*

imposing exact Dirichlet boundary conditions $z = 0$ at $x = -1$ and $x = 1$. Here $z(x)$ denotes the height of the surface. The unique viscosity solution is drawn in Figure 5(a), while a possible weak solution is drawn in Figure 5(b). Our goal is to show that the PSFS equation (2.7) has essentially the same features as the Eikonal equation (3.9), thus showing a similar ambiguity. The starting point is the following proposition.

Proposition 3.1. *The viscosity solution $u = e^v$ of the* PSFS *equation* (2.7) *is increasing along characteristic curves.*

Proof. Let us define

$$\overline{u}(x,y) := \left(I(x,y)\mathsf{f}^2\right)^{-\frac{1}{2}}, \tag{3.10}$$

corresponding to

$$\overline{v}(x,y) := \ln(\overline{u}(x,y)) = -\frac{1}{2}\ln\left(I(x,y)\mathsf{f}^2\right). \tag{3.11}$$

Let us prove that the inequality

$$\overline{u}(x,y) \geq u(x,y) \qquad \forall (x,y) \in \Omega \tag{3.12}$$

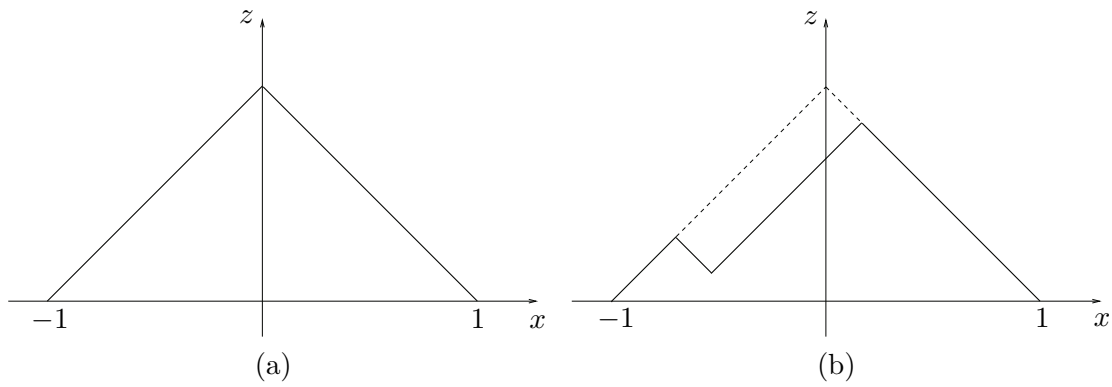

Figure 5. (a) *Viscosity solution and* (b) *a weak solution of the Eikonal equation* (3.9).

(and similarly $\overline{v} \geq v$) holds. Equation (3.12) easily follows from (2.6) and from the definition $u = r/\mathsf{f}$, since $\overline{u}$ is the solution of the equation where $\omega \cdot \widehat{n} = 1$ and it is larger than the solution u where $\omega \cdot \widehat{n} < 1$. In [32] it is also proved that $\overline{v}$ is a supersolution of (2.7). Note that, in the example of Figure 3, the supersolution $\bar{u}$ corresponds to the hemisphere shown in Figure 2.

Let us consider a point (x, y) where v is differentiable (we recall that v is differentiable everywhere in Ω except for a zero-measure subset) and assume that there exists a control $a^* \in \overline{B(0,1)}$ in which the maximum in (2.10) is attained. Then (2.10) can be rewritten as

$$-e^{-2v(x,y)} + (-b(x, y, a^*) \cdot \nabla v(x, y) - \ell(x, y, a^*)) = 0.$$

We have

$$\begin{aligned}
&\frac{\partial v(x,y)}{\partial(-b(x,y,a^*))} = -b(x,y,a^*) \cdot \nabla v(x,y) \\
&= \ell(x,y,a^*) + e^{-2v(x,y)} = -I(x,y)\,\mathsf{f}^2\,\sqrt{1-\|a^*\|^2} + e^{-2v(x,y)} \\
&\geq -I(x,y)\,\mathsf{f}^2\,\sqrt{1-\|a^*\|^2} + e^{-2\overline{v}(x,y)} = I(x,y)\mathsf{f}^2(1-\sqrt{1-\|a^*\|^2}) \geq 0,
\end{aligned}$$

and this proves our assertion. ■

As a consequence of Proposition 3.1, every time the surface we want to reconstruct is described by a function u which is not increasing along characteristics, *it cannot be reconstructed as the viscosity solution of the PSFS equation.* This is exactly what happens in orthographic SFS; see, e.g., [15]. Information spreads from the boundaries to the center of the domain, and the solution can only increase along the way. To overcome this problem (in orthographic SFS as well as PSFS), we can impose the exact solution in every point of local minimum for the solution. Doing this, the correct solution is computed, but we face the new problem of how to recover these values. In this respect, the PSFS model is preferable to the orthographic SFS model, since the light attenuation term $1/r^2$ allows us to get rid of these additional unknowns. Let us explain this point in detail.

According to (3.5), if the surface is differentiable, a local minimum point for u corresponds to a point where $I = 1/r^2$. The latter equation is easily solved for r, and then u is found [36].

This means that the light attenuation term allows us to compute the correct solution exactly where we need to impose it. It turns out from (2.6) that these points are also those where $\omega \cdot \widehat{n} = 1$, which characterizes the so-called *singular points* of the orthographic SFS model [20]. Let us stress that the possibility of computing the correct solution at (differentiable) singular points is a major feature of the PSFS model which distinguishes it from other models in the field.

As we will see in section 4, the numerical resolution of the PSFS equation needs to set up an iterative procedure, and then an initial guess for u has to be given in order to start the algorithm. Let us denote that initial guess by $u^{(0)}$. If we choose $u^{(0)}$ as

$$u^{(0)} := \overline{u}, \tag{3.13}$$

the algorithm starts from a function which is actually the *correct* solution of (2.6) at all points where $\omega \cdot \widehat{n} = 1$, and is *larger* than the correct solution elsewhere. Since the information propagates from the smallest to the largest values, the values larger than the correct ones do not influence the correct ones. Then the values at the local minimum points remain fixed, becoming characteristic sources, while the other values decrease, converging in the limit to the viscosity solution. Note that the initial guess (3.13) corresponds to the initial guess for v suggested in [32], namely

$$v^{(0)} := \overline{v}. \tag{3.14}$$

We conclude that, when the surface is differentiable and local minimum points are not located at the boundary, we can actually solve the PSFS problem with no boundary data and no ambiguity, since the right solution at the local minima can be achieved automatically by choosing a suitable initial guess for the iterative algorithm used to solve the equation.

Otherwise, the method described above cannot always be applied. In particular, the method fails whenever one of the following conditions holds true: (1) a point of nondifferentiability for the surface is a minimum point or (2) local minimum points coincide with the boundaries, and state constraint boundary conditions are used. In these cases, the initial guess (3.13) is not able to impose the right values automatically, and the reconstructed surface will not be the expected one.

In order to explain and summarize the role of the initial guess, the minimum points, and the boundary conditions, it is useful to consider the four surfaces shown in Figure 6. Characteristic curves are depicted below the surfaces (although they lie on Ω). The surface in (a) is differentiable and can be recovered without any additional information. The minimum points for u are automatically detected (black dots on the surface) just by computing $\bar{u}$. Characteristics start from these points, and the solution increases along them. State constraint boundary conditions are suitable since no information comes from the boundaries. The surface in (b) is not differentiable, but the point of nondifferentiability does not coincide with a minimum point for u. Characteristics move away from the minimum points (automatically determined by $\bar{u}$ as before), and they meet each other in the point of nondifferentiability. As in (a), the surface in (b) can be recovered without any additional information. The surface in (c) is differentiable, but it cannot be correctly reconstructed unless suitable Dirichlet boundary conditions are given at the boundary of the domain. Indeed, characteristics start from the automatically detected minimum point, so that the solution u is correctly computed from that

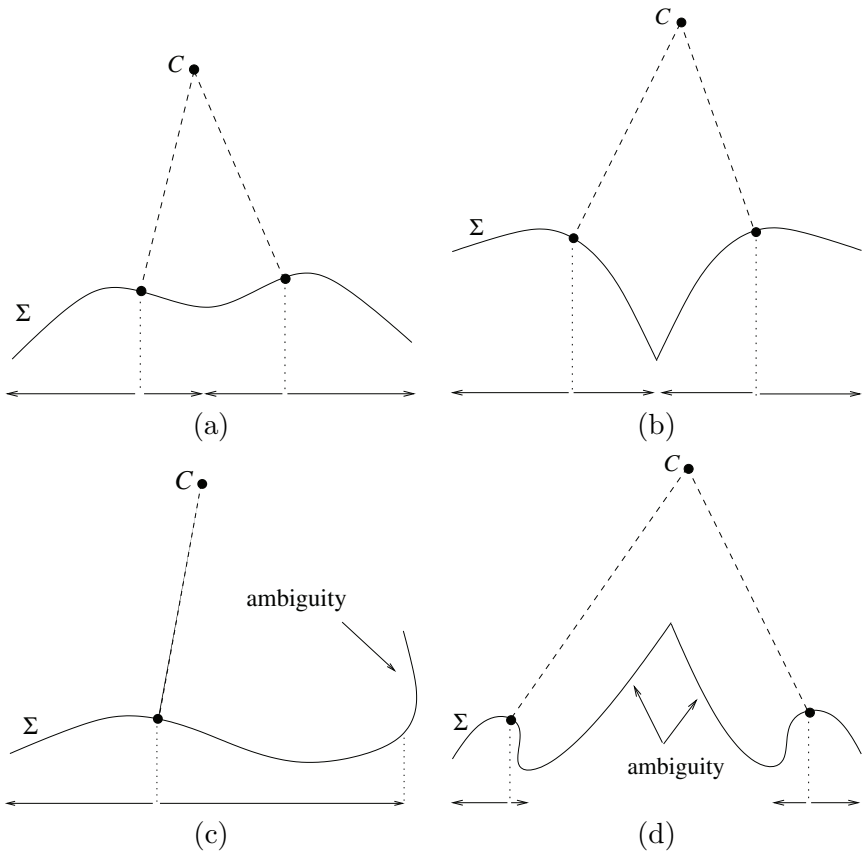

Figure 6. *Four surfaces with different properties. Characteristic curves are depicted below the surfaces.* (a) *Differentiable surface, correctly reconstructed imposing state constraint boundary conditions, starting from the two singular points automatically detected (black dots).* (b) *Nondifferentiable surface, correctly reconstructed as before.* (c) *Differentiable surface with ambiguity if state constraint boundary conditions are imposed. The ambiguity is limited to the region where u should decrease starting from the source points (black dot).* (d) *Nondifferentiable surface with ambiguity. The nondifferentiable point is not recognized as a source by the initial guess.*

point as long as it increases. Imposing state constraint boundary conditions, the viscosity solution to (2.7) near the right-hand boundary corresponds to *another surface with the same brightness function*. The surface in (d) is not differentiable, and the point of nondifferentiability coincides with a minimum point. As the correct computation of minimum points using $\bar{u}$ relies on the differentiability there, this minimum point is not detected, and the viscosity solution to (2.7) does not correspond to this surface on a large part of the domain. Here state constraints are suitable, and the surface is correctly reconstructed near the boundaries. To obtain the correct surface, the value of u at the nondifferentiable point should be given.

At this point it is interesting to compare the classic concave/convex ambiguity in orthographic SFS with the ambiguity shown for PSFS. First, the two ambiguities can both be fixed by assigning the exact value of the solution at the sources of characteristics. Second, they are both caused by an ambiguity in the image irradiance equation (2.3). For the PSFS

equation (2.6), for any ω there is more than one couple $(\widehat{n}, r)$ associated to the same I. This is similar to what happens in the orthographic SFS, where, for any ω, there is more than one $\widehat{n}$ associated to the same I. On the other hand, the concave/convex ambiguity is related to the possible degeneration of the Eikonal equation, which is instead not possible in the PSFS equation with light attenuation term. In fact, for the classical SFS, the right-hand side of the Eikonal equation (3.9) vanishes at singular points, causing a lack of uniqueness even for regular solutions. This situation does not appear in (2.7), due to the presence of the light attenuation term.

Following our previous discussion, we end this section by giving a precise definition of the ambiguity appearing in the PSFS model.

Definition 3.2. *Let Σ and $\widehat{\Sigma}$ be two piecewise continuous surfaces defined on the same domain Ω. Let us denote by Γ and $\widehat{\Gamma}$ their set of discontinuities, respectively. We say that Σ and $\widehat{\Sigma}$ are* ambiguous with respect to the PSFS model with attenuation term (A-ambiguous in short) *if they are piecewise differentiable on $\Omega \setminus \Gamma$ and $\Omega \setminus \widehat{\Gamma}$, respectively, and they are associated to the same brightness function I according to the PSFS model.*

3.3. Some numerical approximations for ambiguous cases. In order to have a numerical confirmation of the theoretical results presented above, we solved the PSFS equation using the scheme presented in [37], which is proved to be convergent in section 4. First, we recovered some of the surfaces described in Figure 3, choosing a constant brightness function I on the same domain Ω and then varying the boundary conditions (state constraint or Dirichlet) or imposing specific values in some internal points. See Figure 7 and its caption.

We have also solved the PSFS problem for two surfaces similar to the surfaces illustrated in Figures 6(c) and 6(d), where an ambiguity is expected. The first surface (see Figure 8(b)) corresponds to $u(x) = \sin(5x) + 5$, $x \in [-0.8, 0.6]$. The second surface (see Figure 9(b)) corresponds to $u(x) = 10|x| + 3$, $x \in [-2, 2]$. For each test we show the initial and the reconstructed surface Σ, together with the functions u and the corresponding brightness functions I. The focal length is set to $\mathsf{f} = 1$, and the discretization steps are chosen to be small enough to reduce the visible approximation errors. We have applied state constraint boundary conditions. We present our numerical results in Figures 8 and 9, respectively.

We see that the first surface is correctly reconstructed in some part of the domain, but the algorithm fails near the right-hand boundary. This is expected because the correct value should be carried by a Dirichlet boundary condition, which is not imposed. The second surface is scarcely reconstructed in its shape, but the result is completely wrong if we compare the scales of the figures (the peak is found at $z \approx -5.5$, while the correct value is $z = -3$). It is useful to note that the example shown in Figure 9 is rather delicate because the ambiguity is generated by the nondifferentiability at a single point. If, for example, we compute the initial brightness function imposing by hand $u'(0) = 0$ (at the discrete level), the minimal point is detected, and the surface is perfectly reconstructed. We stress that the approximate function I (numerically computed by means of the approximate solution u) matches perfectly the exact function I in both cases, confirming the existence of an ambiguity.

It is plain that the ambiguity is not limited to 1-D surfaces. We tried to reconstruct an upside-down pyramid, with Dirichlet boundary conditions imposed at the basis (i.e., the top) of the pyramid. In Figure 10 we show the original surface, the reconstructed surface, and the

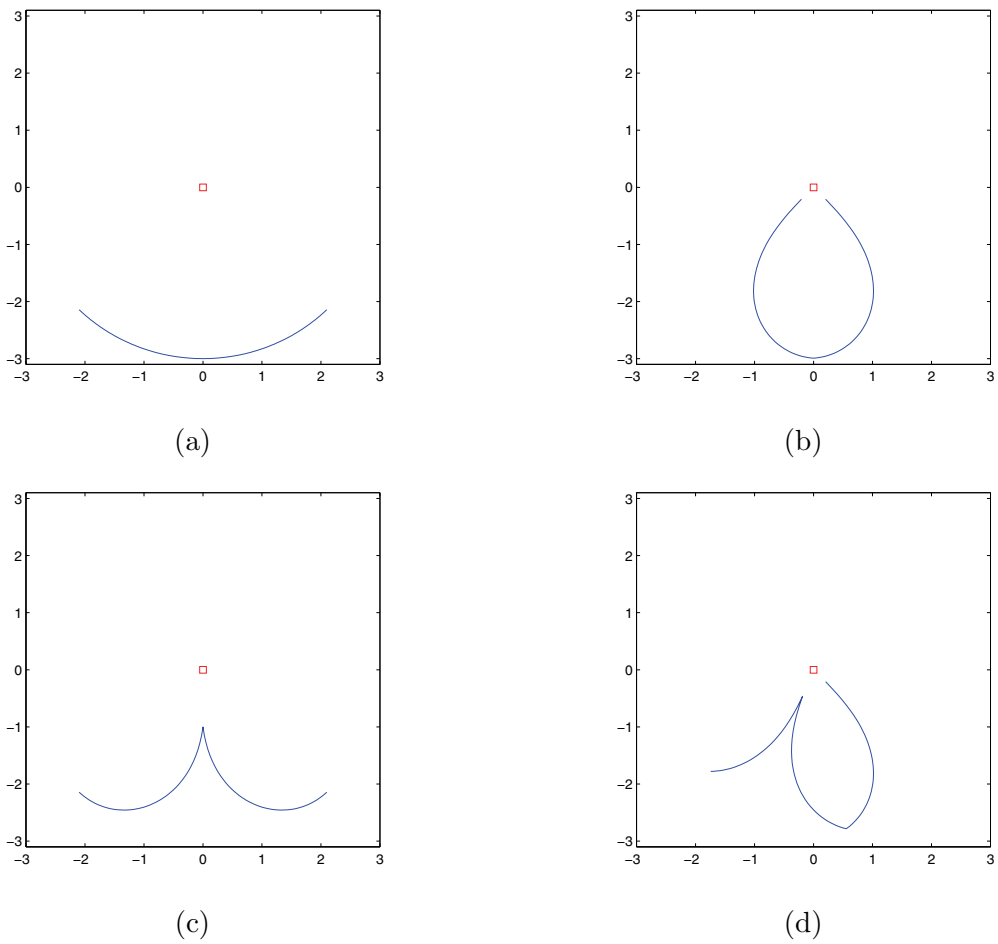

Figure 7. *Some reconstructed surfaces with constant brightness function on the same domain* Ω*:* (a) *with state constraint boundary conditions (convergence is reached in one iteration),* (b) *with a particular Dirichlet boundary condition,* (c) *with state constraint boundary conditions and a specific value imposed at the center, and* (d) *with mixed state constraint and Dirichlet boundary conditions, and a specific value imposed inside the domain. The surfaces* (a), (b), (c) *can be compared, respectively, with those in Figures* 2, 3(c), *and* 4(d), *and the surface* (d) *with a combination of the surfaces in Figures* 4(c) *and* 3(d) *(rotated by a small angle around the optical center, as indicated at the end of section* 3.1*).*

surface reconstructed by imposing an incorrect value at the center of the image, which forces a peak similar to the one in Figure 7(c). We also show the three corresponding brightness functions, which turn out to be identical but for a zero-measure set. The differences are concentrated in the nondifferentiable regions and are due to the numerical approximation of the gradient.

4. Two approximation schemes for the PSFS problem.

The goal of this section is to analyze two approximation schemes that have been proposed in [37] and [14] (as indicated in the introduction, the two schemes will be referred to by the acronyms VBW and CFS, respectively). We study their analytical properties, and we prove that they converge to the

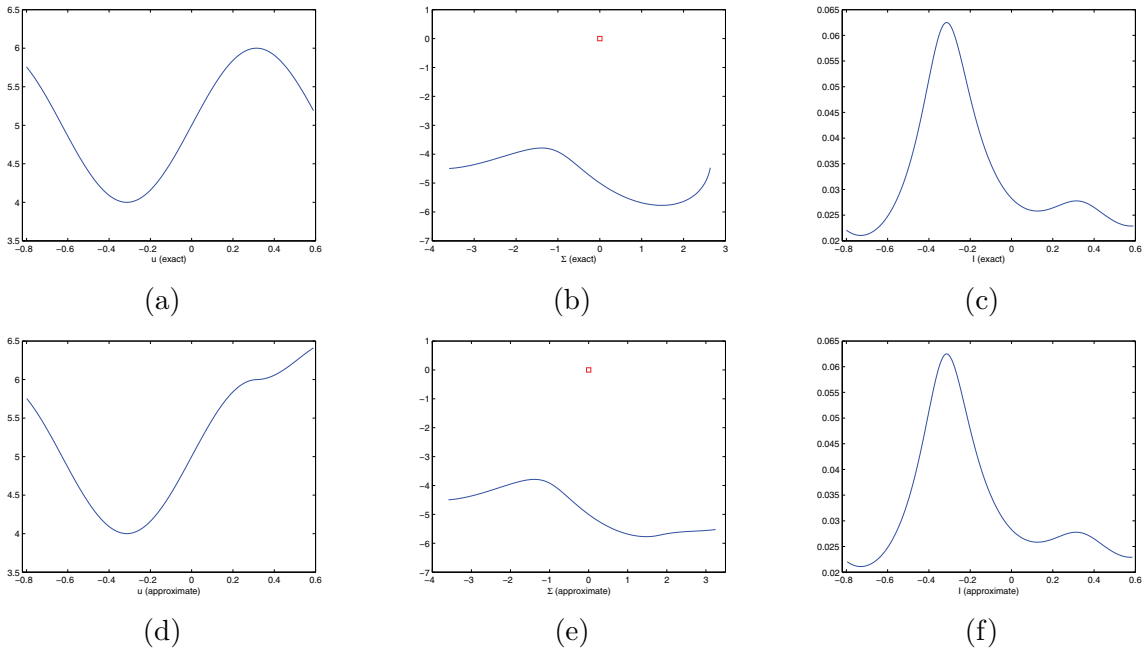

Figure 8. *Numerical outcome for a case similar to that described in Figure* 6(c)*. First row: exact* u*,* Σ*, and* I*. Second row: approximate* u*,* Σ*, and* I*.*

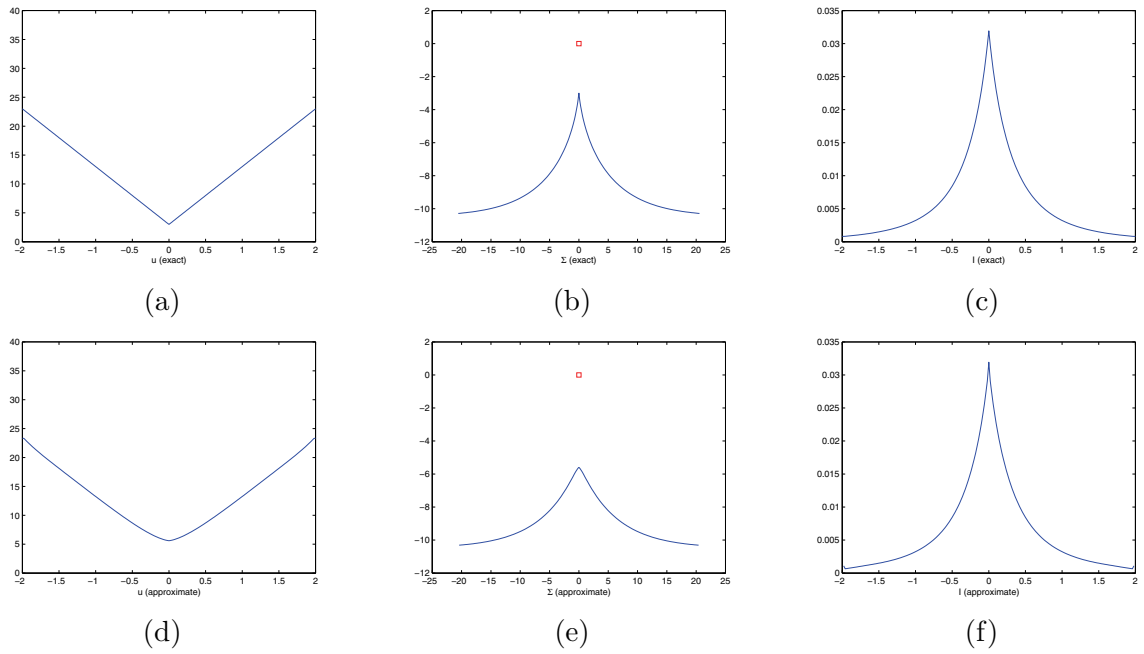

Figure 9. *Numerical outcome for a case similar to that described in Figure* 6(d)*. First row: exact* u*,* Σ*, and* I*. Second row: approximate* u*,* Σ*, and* I*.*

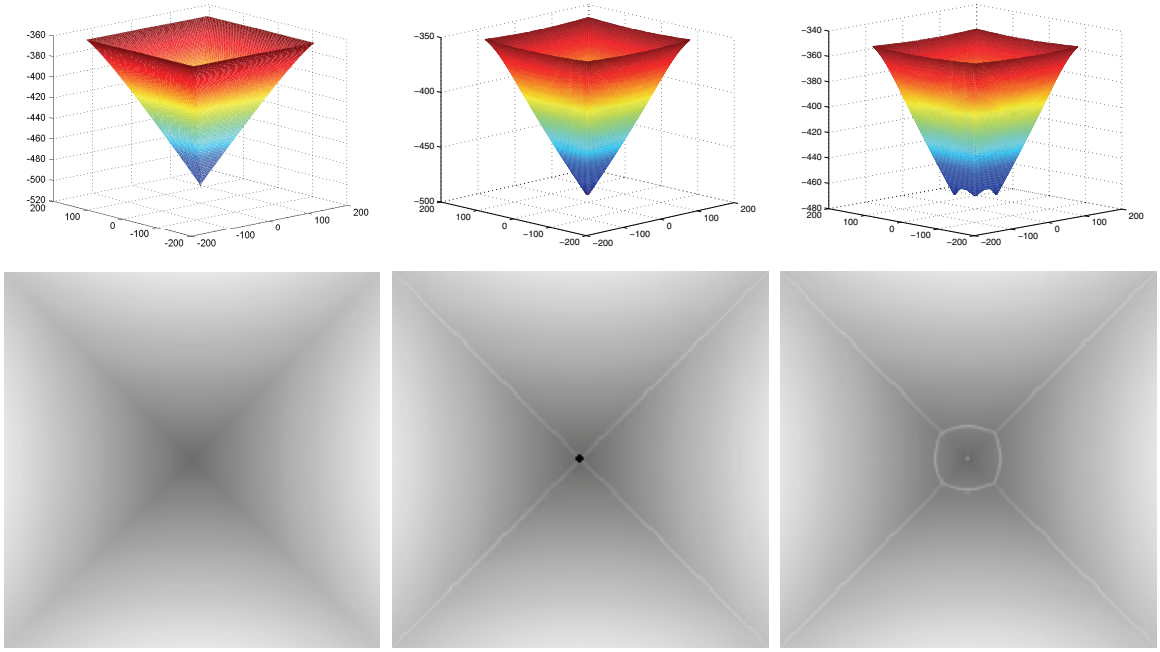

Figure 10. *Top, from left to right: original upside-down pyramid, reconstructed surface, reconstructed surface in the case when a peak is imposed. Bottom: initial image rendered from the upside-down pyramid using the PSFS model, brightness function of the reconstructed surface, brightness function of the reconstructed surface in the case when a peak is imposed.*

viscosity solution of (2.7). Boundary conditions are handled in a standard way for both schemes. We do not mention it explicitly in the text in order to simplify the presentation. We refer the interested reader to [6] for a detailed comparison of the performances of these schemes. Experimental evidence shows that all the schemes available for the PSFS equation compute comparable solutions, although relevant differences appear in the accuracy and CPU time.

4.1. The VBW scheme: Properties and convergence. In this section we describe the VBW scheme, which is the scheme we used in the simulations presented in the previous section. We prove the convergence of the approximate solution to the viscosity solution of (2.7) when the discretization step goes to zero.

In order to simplify the presentation, we first prove the properties of the scheme in one dimension. Then, we will point out how the proofs can be extended to two dimensions.

1-D analysis. Let us introduce the discretization of the spatial derivative made by means of the upwind method as in Rouy and Tourin [33]. Let $\Delta x > 0$ be the spatial mesh width in the x direction and denote by $N = N(\Delta x)$ the number of mesh points x_i, $i = 1, \dots, N$. Denote by w_i the approximate value of v at the ith mesh point x_i and define $\phi_i(w)$ as

$$\phi_i(w) := \min\left(0, \frac{w_{i+1} - w_i}{\Delta x}, \frac{w_{i-1} - w_i}{\Delta x}\right), \quad i = 1, \dots, N, \tag{4.1}$$

where $w = (w_1, \dots, w_N)$. The approximate gradient is given by

$$\nabla v(x_i) \approx \widetilde{\nabla} w_i := \begin{cases} -\phi_i(w) & \text{if } \phi_i(w) = \frac{w_{i-1}-w_i}{\Delta x}, \\ \phi_i(w) & \text{otherwise.} \end{cases} \tag{4.2}$$

By the above upwind discretization, one gets the discrete operator

$$L_i(w) := \left(-\frac{I_i \mathsf{f}^2}{Q_i} \sqrt{(\mathsf{f}\widetilde{\nabla} w_i)^2 + (x_i \widetilde{\nabla} w_i)^2 + Q_i^2} + e^{-2w_i} \right) \tag{4.3}$$

and can write the discrete version of (2.7) as

$$L_i(w) = 0, \quad i = 1, \dots, N. \tag{4.4}$$

Let us introduce the parameter $\tau > 0$ and the function $G^\tau : \mathbb{R}^N \to \mathbb{R}^N$ defined componentwise as follows:

$$G_i^\tau(w) := w_i + \tau L_i(w), \qquad i = 1, \dots, N. \tag{4.5}$$

Equation (4.4) can be written in fixed point form as

$$w = G^\tau(w). \tag{4.6}$$

Note that $G_i^\tau \in C^0(\mathbb{R}^N)$ and is piecewise differentiable in $\mathbb{R}^N$. We describe important structural properties of G^τ in the following proposition.

Proposition 4.1. *Let $G^\tau : \mathbb{R}^N \to \mathbb{R}^N$ be defined as in (4.5) and let $w', w'' \in \mathbb{R}^N$. Then, there exists $\tau^* = \tau^*(\Delta x) > 0$ such that*

(i) *$w' \le w''$ implies $G^\tau(w') \le G^\tau(w'')$ for any $\tau < \tau^*$ ($\le$ is intended componentwise);*

(ii) *$\|G^\tau(w') - G^\tau(w'')\|_\infty < \|w' - w''\|_\infty$ for any $\tau < \tau^*$.*

Proof. Let us first assume that the evaluation of (4.2) gives $\widetilde{\nabla} w_i = \frac{w_i - w_{i-1}}{\Delta x}$, which implies $w_i - w_{i-1} > 0$. Then, we have

$$\frac{\partial G_i^\tau(w)}{\partial w_i} = 1 - \frac{\tau I_i \mathsf{f}^2}{Q_i} \frac{(x_i^2 + \mathsf{f}^2)\frac{w_i - w_{i-1}}{\Delta x^2}}{\sqrt{(\mathsf{f}^2 + x_i^2)\left(\frac{w_i - w_{i-1}}{\Delta x}\right)^2 + Q_i^2}} - 2\tau e^{-2w_i}, \tag{4.7}$$

$$\frac{\partial G_i^\tau(w)}{\partial w_{i-1}} = \frac{\tau I_i \mathsf{f}^2}{Q_i} \frac{(x_i^2 + \mathsf{f}^2)\frac{w_i - w_{i-1}}{\Delta x^2}}{\sqrt{(\mathsf{f}^2 + x_i^2)\left(\frac{w_i - w_{i-1}}{\Delta x}\right)^2 + Q_i^2}}, \tag{4.8}$$

and

$$\frac{\partial G_i^\tau(w)}{\partial w_{i+1}} = 0. \tag{4.9}$$

The term $\partial G_i^\tau(w)/\partial w_{i-1}$ is always positive, whereas $\partial G_i^\tau(w)/\partial w_i$ is positive only for τ sufficiently small. Note that the maximal value τ^* can be explicitly computed by means of (4.7), and the condition $\tau < \tau^*$ can be explicitly verified while the algorithm is running.

If $\widetilde{\nabla} w_i = \frac{w_{i+1}-w_i}{\Delta x}$, we get a similar result. Let us assume now that $\widetilde{\nabla} w_i = 0$. We get

$$G_i^\tau(w) = w_i - \tau I_i \mathsf{f}^2 + \tau e^{-2w_i}$$

and then

$$\frac{\partial G_i^\tau(w)}{\partial w_i} = 1 - 2\tau e^{-2w_i}\,, \quad \frac{\partial G_i^\tau(w)}{\partial w_{i-1}} = \frac{\partial G_i^\tau(w)}{\partial w_{i+1}} = 0.$$

Again, the three terms are positive, provided that τ is sufficiently small. This proves (i).

Let us denote by J_{G^τ} the Jacobian matrix of G^τ. Whatever the evaluation of $\widetilde{\nabla} w$ gives, assuming that τ is sufficiently small, we get

$$\|J_{G^\tau}\|_\infty = \max_i \left\{ \frac{\partial G_i^\tau}{\partial w_{i-1}} + \frac{\partial G_i^\tau}{\partial w_i} + \frac{\partial G_i^\tau}{\partial w_{i+1}} \right\} = \max_i \left\{ 1 - 2\tau e^{-2w_i} \right\}, \tag{4.10}$$

which is always strictly lower than 1, and this ends the proof. ■

The algorithm is implemented in the following iterative form:

$$w_i^{(n+1)} = G_i^\tau(w^{(n)})\,, \qquad i = 1, \dots, N, \quad n = 0, 1, \dots. \tag{4.11}$$

The initial guess $w^{(0)}$ is given by the discretization of (3.14).

Proposition 4.2. *Let $w^{(0)}$ be chosen as in (3.14) and let τ^* be the "constant" defined by Proposition 4.1. Then, there exists $\tau^{**} = \tau^{**}(\Delta x) > 0$ such that*

(i) *the algorithm (4.11) converges to the unique fixed point $\widehat{w}^{\Delta x}$ for any $\tau < \tau^{**}$;*

(ii) *if $\tau < \min\{\tau^*, \tau^{**}\}$, the algorithm converges monotonically decreasing; i.e., for any $i = 1, \dots, N$, we have $w_i^{(n+1)} \le w_i^{(n)}$, $n = 0, 1, \dots$.*

Proof. In order to apply the Banach fixed point theorem, we have only to show that $G^\tau : X \to X$, where X is a *compact* subset of $\mathbb{R}^N$. We choose $X = [w_{\min}, w_{\max}]^N$, where $w_{\min}$ and $w_{\max}$ are two constants such that $w_{\min} < -\frac{1}{2}\ln(I_i \mathsf{f}^2)$ and $w_{\max} > -\frac{1}{2}\ln(I_i \mathsf{f}^2)$ for any $i = 1, \dots, N$. This ensures that

$$-I_i \mathsf{f}^2 + e^{-2w_{\min}} > 0 \quad \text{for any } i \tag{4.12}$$

and

$$-I_i \mathsf{f}^2 + e^{-2w_{\max}} < 0 \quad \text{for any } i. \tag{4.13}$$

Let us fix $w \in X$ and $i \in \{1, \dots, N\}$. The proof is divided into two steps.

(a) We prove that $G_i^\tau(w) \ge w_{\min}$. We have $w_i = w_{\min} + \delta$ for some $0 \le \delta \le \delta_{\max}$ with $\delta_{\max} := w_{\max} - w_{\min}$. Since all the components of w are larger than $w_{\min}$, using (4.2) we get $(\widetilde{\nabla} w_i)^2 \le (\frac{\delta}{\Delta x})^2$. Then we have

$$G_i^\tau(w) = w_i + \tau L_i(w) \ge w_{\min} + \delta + \tau \Psi_1(\delta),$$

where

$$\Psi_1(\delta) := \left(-\frac{I_i \mathsf{f}^2}{Q_i} \sqrt{\left(\mathsf{f}\frac{\delta}{\Delta x}\right)^2 + \left(x_i \frac{\delta}{\Delta x}\right)^2 + Q_i^2} + e^{-2(w_{\min}+\delta)} \right).$$

Given (4.12), we know that $\Psi_1(0) = -I_i\mathsf{f}^2 + e^{-2w_{\min}} > 0$. The function $\Psi_1(\delta)$ is monotonically decreasing, and $\lim_{\delta\to+\infty}\Psi_1(\delta) = -\infty$. As a consequence, there exists a unique $\delta_0 > 0$ such that $\Psi_1(\delta_0) = 0$. If $0 \le \delta \le \delta_0$, we have $\Psi_1(\delta) \ge 0$ and $G_i^\tau(w) \ge w_{\min}$ for any τ. Otherwise, if $\delta_0 < \delta \le \delta_{\max}$, we choose

$$\tau \le \frac{\delta_0}{-\Psi_1(\delta_{\max})},$$

which guarantees $\tau \le \frac{\delta}{-\Psi_1(\delta)}$, and we easily conclude.

(b) Let us now prove that $G_i^\tau(w) \le w_{\max}$. Similarly as before, we have $w_i = w_{\max} - \delta$ for some $0 \le \delta \le \delta_{\max}$ with $\delta_{\max} := w_{\max} - w_{\min}$. Then we have

$$G_i^\tau(w) = w_i + \tau L_i(w) \le w_{\max} - \delta + \tau\Psi_2(\delta),$$

where

$$\Psi_2(\delta) := \left(-\frac{I_i\mathsf{f}^2}{Q_i}\sqrt{0+0+Q_i^2} + e^{-2(w_{\max}-\delta)}\right) = \left(-I_i\mathsf{f}^2 + e^{-2(w_{\max}-\delta)}\right).$$

Given (4.13), we know that $\Psi_2(0) = -I_i\mathsf{f}^2 + e^{-2w_{\max}} < 0$. The function $\Psi_2(\delta)$ is monotonically increasing, and $\lim_{\delta\to+\infty}\Psi_2(\delta) = +\infty$. As a consequence, there exists a unique $\delta_0 > 0$ such that $\Psi_2(\delta_0) = 0$. If $0 \le \delta \le \delta_0$, we have $\Psi_2(\delta) \le 0$ and $G_i^\tau(w) \le w_{\max}$ for any τ. Otherwise, if $\delta_0 < \delta \le \delta_{\max}$, we choose

$$\tau \le \frac{\delta_0}{\Psi_2(\delta_{\max})},$$

which guarantees $\tau \le \frac{\delta}{\Psi_2(\delta)}$, and we easily conclude. This proves Proposition 4.2(i).

The choice of the initial guess is the key property in obtaining monotone decreasing convergence to the fixed point. In fact, $w^{(0)}$ is larger than (or equal to) the solution (see section 3.2), and G^τ verifies Proposition 4.1(i). This proves Proposition 4.2(ii). ■

We want to prove convergence of the numerical solution $\widehat{w}^{\Delta x}$ to the viscosity solution v of (2.7) for $\Delta x \to 0$. We can rely on the classic results of Barles and Souganidis [2], following the same strategy of Rouy and Tourin [33].

Proposition 4.3. *Let $w^{(0)}$ be chosen as in (3.14) and let τ^*, τ^{**} be the "constants" defined by Propositions 4.1 and 4.2. If $\tau < \min\{\tau^*, \tau^{**}\}$, then the algorithm (4.11) converges to $\widehat{w}^{\Delta x}$ for $n \to +\infty$, and $\widehat{w}^{\Delta x}$ converges locally uniformly to v for $\Delta x \to 0$.*

Proof. Convergence to $\widehat{w}^{\Delta x}$ for $n \to +\infty$ is proved in Proposition 4.2(i). To prove the convergence to v, we start proving that the scheme is monotone in the sense given in [2]. We know that the fixed point $\widehat{w}^{\Delta x}$ satisfies the equation

$$L(w) = 0,$$

so we will use this form, since in [2] the discrete operator is written in the implicit form $S(\Delta x, x, w(x), w) = 0$, where $S : \mathbb{R}^+ \times \overline{\Omega} \times \mathbb{R} \times B(\overline{\Omega}) \to \mathbb{R}$ and $B(\overline{\Omega})$ is the space of bounded functions defined on $\overline{\Omega}$. If the evaluation of (4.2) gives $\widetilde{\nabla} w_i = \frac{w_i - w_{i-1}}{\Delta x}$, we have only to prove that $\frac{\partial L_i(w)}{\partial w_{i-1}}$ does not change sign. By (4.8) we easily get $\frac{\partial L_i(w)}{\partial w_{i-1}} > 0$. If the evaluation of (4.2) gives $\widetilde{\nabla} w_i = \frac{w_{i+1} - w_i}{\Delta x}$, we obtain analogously $\frac{\partial L_i(w)}{\partial w_{i+1}} > 0$. Finally, if $\widetilde{\nabla} w_i = 0$, L_i does not depend on w_{i-1} or w_{i+1}.

The *stability* and *consistency* of the scheme are easy to prove. Since the *comparison principle* for the problem is proved in [32], we know that (2.7) has a unique viscosity solution v, and we can conclude, by the general convergence result in [2], that the approximate solution converges locally uniformly to v. ■

It is interesting to note that the property pointed out in Proposition 3.1 is preserved in the numerical approximation. Let us assume that the assumptions of Proposition 4.3 are satisfied. We want to show that

$$\begin{cases} w_i^{(n+1)} > w_{i-1}^{(n)} & \text{if } \widetilde{\nabla} w_i = \frac{w_i - w_{i-1}}{\Delta x}, \\ w_i^{(n+1)} > w_{i+1}^{(n)} & \text{if } \widetilde{\nabla} w_i = \frac{w_{i+1} - w_i}{\Delta x}, \\ w_i^{(n+1)} = w_i^{(n)} & \text{if } \widetilde{\nabla} w_i = 0. \end{cases} \tag{4.14}$$

If (4.14) holds true, the solution is constructed from the smallest to the largest values, and then the solution cannot become lower than the information sources (Dirichlet boundary conditions or minimum points automatically detected). Let us prove the first line in (4.14). To this end, we first recall that

$$w_i^{(n+1)} = G_i^\tau(w^{(n)}) = w_i^{(n)} + \tau L_i(w^{(n)}).$$

Note that Proposition 4.2(ii) implies $L_i(w^{(n)}) < 0$ for any i and n. In order to have $w_i^{(n+1)} > w_{i-1}^{(n)}$, the parameter τ must be chosen in such a way that

$$\tau |L(w^{(n)})| < w_i^{(n)} - w_{i-1}^{(n)},$$

which corresponds to

$$\tau < \frac{w_i^{(n)} - w_{i-1}^{(n)}}{-L_i(w^{(n)})}. \tag{4.15}$$

Note that the right-hand term in (4.15) is strictly positive. For any fixed Δx, the term $L_i(w^{(n)}) \to 0$ when $n \to +\infty$ (this follows by the fact that the algorithm converges to the fixed point). Then, condition (4.15) is always satisfied in the limit.

We can also reobtain the result already proved for the continuous equation. Let us write

$$\frac{w_i^{(n+1)} - w_{i-1}^{(n)}}{\Delta x} = \frac{w_i^{(n+1)} - w_i^{(n)}}{\Delta x} + \frac{w_i^{(n)} - w_{i-1}^{(n)}}{\Delta x}.$$

Since, as we have just seen, $w_i^{(n+1)} - w_{i-1}^{(n)} \geq 0$, and we know that $w_i^{(n+1)} - w_i^{(n)} \leq 0$ (because the algorithm computes a decreasing sequence), we obtain that $w_i^{(n)} - w_{i-1}^{(n)} \geq 0$ for any Δx, and then, passing to the limit (in the case it exists),

$$\lim_{\Delta x \to 0^+} \frac{w(x_i) - w(x_i - \Delta x)}{\Delta x} \geq 0,$$

which corresponds to the fact that the solution is increasing along the characteristic direction.

2-D analysis. The strategy developed in the 1-D case can be easily generalized, and all the main results still hold. The only difference is a new condition on the experimental set-up which is necessary to prove that $w_1 \leq w_2$ implies $G^\tau(w_1) \leq G^\tau(w_2)$.

Assuming a square uniform $N \times N$ grid with $\Delta x = \Delta y$, the scheme is now defined componentwise by

$$G^\tau_{i,j}(w) := w_{i,j} + \tau L_{i,j}(w), \qquad i,j = 1,\dots,N, \tag{4.16}$$

where

$$L_{i,j}(w) := -\frac{I_{i,j}}{Q_{i,j}}\mathsf{f}^2\sqrt{\mathsf{f}^2\left((\widetilde{\nabla}_x w_{i,j})^2 + (\widetilde{\nabla}_y w_{i,j})^2\right) + \left(x_i\widetilde{\nabla}_x w_{i,j} + y_j\widetilde{\nabla}_y w_{i,j}\right)^2 + Q^2_{i,j}} + e^{-2w_{i,j}}. \tag{4.17}$$

Let us assume that $\widetilde{\nabla} w_{i,j}$ is equal to $\frac{1}{\Delta x}\left(w_{i,j} - w_{i-1,j}, w_{i,j} - w_{i,j-1}\right)$. We have

$$\frac{\partial G^\tau_{i,j}(w)}{\partial w_{i-1,j}} = \frac{\tau I_{i,j}\mathsf{f}^2}{Q_{i,j}}\frac{A_{ij}(w)}{\sqrt{B_{ij}(w)}}, \tag{4.18}$$

where

$$A_{ij}(w) := (x_i^2 + \mathsf{f}^2)\frac{w_{i,j} - w_{i-1,j}}{\Delta x^2} + x_i y_j \frac{w_{i,j} - w_{i,j-1}}{\Delta x^2}, \tag{4.19}$$

$$\begin{aligned} B_{ij}(w) := {} & \mathsf{f}^2\left(\frac{w_{i,j} - w_{i-1,j}}{\Delta x}\right)^2 + \mathsf{f}^2\left(\frac{w_{i,j} - w_{i,j-1}}{\Delta x}\right)^2 \\ & + \left(x_i\frac{w_{i,j} - w_{i-1,j}}{\Delta x} + y_j\frac{w_{i,j} - w_{i,j-1}}{\Delta x}\right)^2 + Q^2_{i,j}, \end{aligned} \tag{4.20}$$

and an analogous result for $\partial G^\tau_{i,j}(w)/\partial w_{i,j-1}$. With no further assumptions, the quantity in (4.18) can be negative, due to the term $x_i y_j$ in (4.19), which has no fixed sign. Then, in order to get the same result as in the 1-D case, namely $\|J_{G^\tau}\|_\infty = \max_{i,j}\left\{1 - 2\tau e^{-2w_{i,j}}\right\}$, we need to assume that

$$(x_i^2 + \mathsf{f}^2)\left(w_{i,j} - w_{i-1,j}\right) + x_i y_j\left(w_{i,j} - w_{i,j-1}\right) \geq 0 \tag{4.21}$$

and, analogously, that

$$(y_j^2 + \mathsf{f}^2)\left(w_{i,j} - w_{i,j-1}\right) + x_i y_j\left(w_{i,j} - w_{i-1,j}\right) \geq 0. \tag{4.22}$$

As the conditions (4.21)–(4.22) incorporate a coupling of image dimension and focal length, they imply a condition on the experimental set-up. They are fulfilled if f is sufficiently large, or if the surface is fully contained in the "positive" region $\{x > 0,\ y > 0\}$.

4.2. The CFS scheme: Properties and convergence. In order to simplify the notation, let us prove the result in the 1-D case. Generalization to a higher dimension is trivial, and all the results are preserved. The semidiscrete formulation of the CFS scheme was derived in [13, 14]; we report it here for the reader's convenience. For any function $w : \mathbb{R} \to \mathbb{R}$, we define the semidiscrete operator F^h as

$$F^h[w](x) := \min_{a \in \overline{B(0,1)}} \{w(x + hb(x,a)) + h\ell(x,a)\} + he^{-2w(x)}. \tag{4.23}$$

The iterative algorithm can be written in compact form as

$$\begin{cases} w^{(n+1)}(x) = F^h[w^{(n)}](x)\,, & n = 0, 1, \dots, \\ w^{(0)}(x) = -\frac{1}{2}\ln(I(x)\mathsf{f}^2). \end{cases} \tag{4.24}$$

As usual, the parameter h must be intended as a fictitious-time discretization step used to integrate along characteristics in the semi-Lagrangian formulation [18]. We do not consider here the fully discrete problem in which the operator F^h is projected on a grid.

In the following we prove that the sequence generated by the algorithm (4.24) actually converges to some function w^h. Note that we employ here an approach that is different from the one used in the previous subsection for the analysis of the VBW method. More precisely, we will *not* prove that the operator F^h is a contraction mapping, but we prove that the sequence $\{w^{(n)}\}_{n\geq 0}$ is monotone decreasing and bounded from below.

Proposition 4.4 (boundedness from below). *Let $w \in C^0(\Omega)$. For any $x \in \Omega$ there exist a step $h = h(x) > 0$ and a constant $w_{\min} \in \mathbb{R}$ such that*

$$w(x) \geq w_{\min} \quad \textit{implies} \quad F^h[w](x) \geq w_{\min}. \tag{4.25}$$

Proof. Let us consider two cases separately.

(i) Let $w(x) = w_{\min}$. We first note, by the definition of ℓ in (2.11), that $\ell(x,0) = \min_a\{\ell(x,a)\}$. Second, by the definition of b in (2.11), we have $w(x + hb(x,0)) = w(x) = \min_a\{w(x + hb(x,a))\}$ since the minimum of w is attained at x by assumption. As a consequence, the minimum in (4.23) is attained for $a^* = 0$. Then,

$$F^h[w](x) = w(x) - hI(x)\mathsf{f}^2 + he^{-2w(x)} = w_{\min} + h\left(e^{-2w_{\min}} - I(x)\mathsf{f}^2\right).$$

Similarly to the VBW case, we choose $w_{\min}$ in such a way that

$$e^{-2w_{\min}} - I(x)\mathsf{f}^2 \geq 0,$$

and then $F^h[w](x) \geq w_{\min}$. Note that it is possible to choose such a $w_{\min}$ uniformly in x. To this end, it is sufficient to choose $w_{\min} \leq \min_{x\in\Omega} w^{(0)}(x)$.

(ii) Let $w(x) > w_{\min}$. The continuity of w guarantees that there exists a ball $B(x,\xi)$ centered in x of radius ξ such that $w(x') > w_{\min}$ for every $x' \in B(x,\xi)$. Let us denote by a^* the arg min appearing in the definition of $F^h[w]$. Defining $\Delta w = w(x + hb(x,a^*)) - w_{\min}$, we have

$$\begin{aligned} F^h[w](x) &= w(x + hb(x,a^*)) + h\ell(x,a^*) + he^{-2w(x)} \\ &= w_{\min} + \Delta w + h(e^{-2w(x)} + \ell(x,a^*)) \\ &\geq w_{\min} + \Delta w + h(0 - I(x)\mathsf{f}^2). \end{aligned}$$

Choosing h in such a way that $h \max_a b(x,a) < \xi$, we have $\Delta w > 0$. Moreover, we note that Δw does not tend to zero if h tends to zero. The conclusion follows by choosing $h \leq \Delta w / I(x)\mathsf{f}^2$. ■

Proposition 4.5 (monotonicity). *Let us assume that $w^{(n)} \in C^1(\Omega)$ for any $n \in \mathbb{N}$. Then, for any $n \in \mathbb{N}$ there exists a step $h = h(n) > 0$ such that the sequence defined in (4.24) verifies*

$$w^{(n+1)}(x) \leq w^{(n)}(x) \quad \textit{for any } x \in \Omega.$$

Proof. We first consider points x such that the corresponding a^* is equal to zero at the first iteration $n = 0$. These are the points where the initial guess $w^{(0)}$ is actually the correct solution; see section 3.2. In this case we have

$$w^{(1)}(x) = w^{(0)}(x) - hI(x)\mathsf{f}^2 + he^{-2w^{(0)}(x)} = w^{(0)}(x).$$

Since the solution already reached convergence at these points, we can simply stop the computation (so that $w^{(n+1)}(x) = w^{(n)}(x)$ for any n).

Let us now consider a point x such that $a^*(x) \neq 0$ for $n = 0$. We prove the assertion by induction on n. We have

$$w^{(1)}(x) = w^{(0)}(x + hb(x,a^*)) + h\ell(x,a^*) + he^{-2w^{(0)}(x)}.$$

Since $a^* \neq 0$, we have

$$w^{(0)}(x + hb(x,a^*)) + h\ell(x,a^*) < w^{(0)}(x + hb(x,0)) + h\ell(x,0) = w^{(0)}(x) - hI(x)\mathsf{f}^2, \tag{4.26}$$

and then $w^{(1)}(x) < w^{(0)}(x) - hI(x)\mathsf{f}^2 + he^{-2w^{(0)}(x)} = w^{(0)}(x)$. Note that we could find two different optimal controls $a_1^* = 0$ and $a_2^* \neq 0$ in which the minimum is attained, so that the strict inequality in (4.26) does not hold true. This issue can be fixed assuming that in such an ambiguous case we keep a_1^* as optimal control.

Now we prove that

$$w^{(n)}(x) < w^{(n-1)}(x) \text{ implies } w^{(n+1)}(x) < w^{(n)}(x).$$

We have to prove that $F^h[w^{(n)}](x) < F^h[w^{(n-1)}](x)$. Let us denote by a^* the arg min for $F^h[w^{(n-1)}](x)$. Note that a^* is in general different from the arg min for $F^h[w^{(n)}](x)$. Then, it is sufficient to show that

$$\begin{aligned} &w^{(n)}(x + hb(x,a^*)) + h\ell(x,a^*) + he^{-2w^{(n)}(x)} \\ &< w^{(n-1)}(x + hb(x,a^*)) + h\ell(x,a^*) + he^{-2w^{(n-1)}(x)} \end{aligned}$$

or, analogously, that

$$w^{(n)}(x + hb(x,a^*)) - w^{(n-1)}(x + hb(x,a^*)) + h\Big(e^{-2w^{(n)}(x)} - e^{-2w^{(n-1)}(x)}\Big) < 0.$$

Since the function $z \mapsto e^{-2z}$ is differentiable and $w^{(n)}(x) \geq w_{\min}$ for any n (see Proposition 4.4), by Taylor's expansion we get

$$\Big(e^{-2w^{(n)}(x)} - e^{-2w^{(n-1)}(x)}\Big) < 2e^{-2w_{\min}}\Big(w^{(n-1)}(x) - w^{(n)}(x)\Big).$$

Then, we need only prove that

$$w^{(n)}(x + hb(x, a^*)) - w^{(n-1)}(x + hb(x, a^*)) + 2he^{-2w_{\min}}\Big(w^{(n-1)}(x) - w^{(n)}(x)\Big) < 0.$$

Let us define $C := 2e^{-2w_{\min}}$ and again use Taylor's expansion for $w^{(n)}$ and $w^{(n-1)}$. We have

$$\begin{aligned}(1 - Ch)w^{(n)}(x) + (Ch - 1)w^{(n-1)}(x)\\ + hb(x, a^*) \cdot \Big(\nabla w^{(n)}(x) - \nabla w^{(n-1)}(x)\Big) + O(h^2) < 0.\end{aligned} \tag{4.27}$$

When h tends to zero, the left-hand side of the previous inequality tends to $w^{(n)}(x) - w^{(n-1)}(x)$, which is strictly negative by assumption. Then there exists an h sufficiently small such that (4.27) holds true. ■

To conclude, let us observe that, assuming $I \in C^1(\Omega)$, we have $w^{(0)} \in C^1(\Omega)$ and then $w^{(n)} \in C^1(\Omega)$ for any n, since the regularity is preserved by the operator F^h. Under this assumption, the two previous propositions can be applied, and we get the convergence of the sequence defined in (4.24).

Finally, note that the dependence of the step h on x and n is not an issue in the implementation of the numerical approximation because the space is discretized in a finite number of nodes and the algorithm is stopped after a finite number of iterations.

5. Dealing with discontinuous surfaces.

In this section we suggest a simple algorithm to deal with the reconstruction of *discontinuous surfaces*. Discontinuous surfaces can arise both because of different objects in a scene and because of parts of the object being occluded by other parts of the object due to the projection. Numerical tests performed in [6, 13, 14] clearly show that the PSFS algorithm is not able to catch discontinuities of the surface. In fact, it tries to reconstruct a continuous surface with the same brightness function as the original one. In order to deal with discontinuities, the idea is to first perform a segmentation of the input image, dividing the domain into several subdomains. The boundaries of the subdomains correspond to the curves of discontinuity of the brightness function. Then, we apply the PSFS algorithm piecewise in every subdomain where the brightness function is continuous. For each subdomain, initial data for the iterative schemes are chosen as in (3.14).

It is worth noting that a similar segmentation procedure will not be valid for the orthographic SFS problem. Indeed, splitting the original image into subdomains will result in an even more complicated problem where several new boundaries have to be taken into account. Since in the orthographic SFS model the gray values do not contain depth information, if no additional information is available, the segmented SFS problem will be undetermined.

The question arises of which boundary conditions have to be imposed at the boundary of each subdomain for the PSFS model. In the following we have always imposed state constraint boundary conditions there. This is a natural choice, since they simply inhibit the propagation of information from outside the segment into the segment. This makes sense, since any information from outside the segment, i.e., across the discontinuity, is unreliable. To impose state constraint boundary conditions on each segment we simply set on the boundary of the segment a value larger than the maximal value of the solution inside the segment. An easy choice is to set it equal to the maximum machine number.

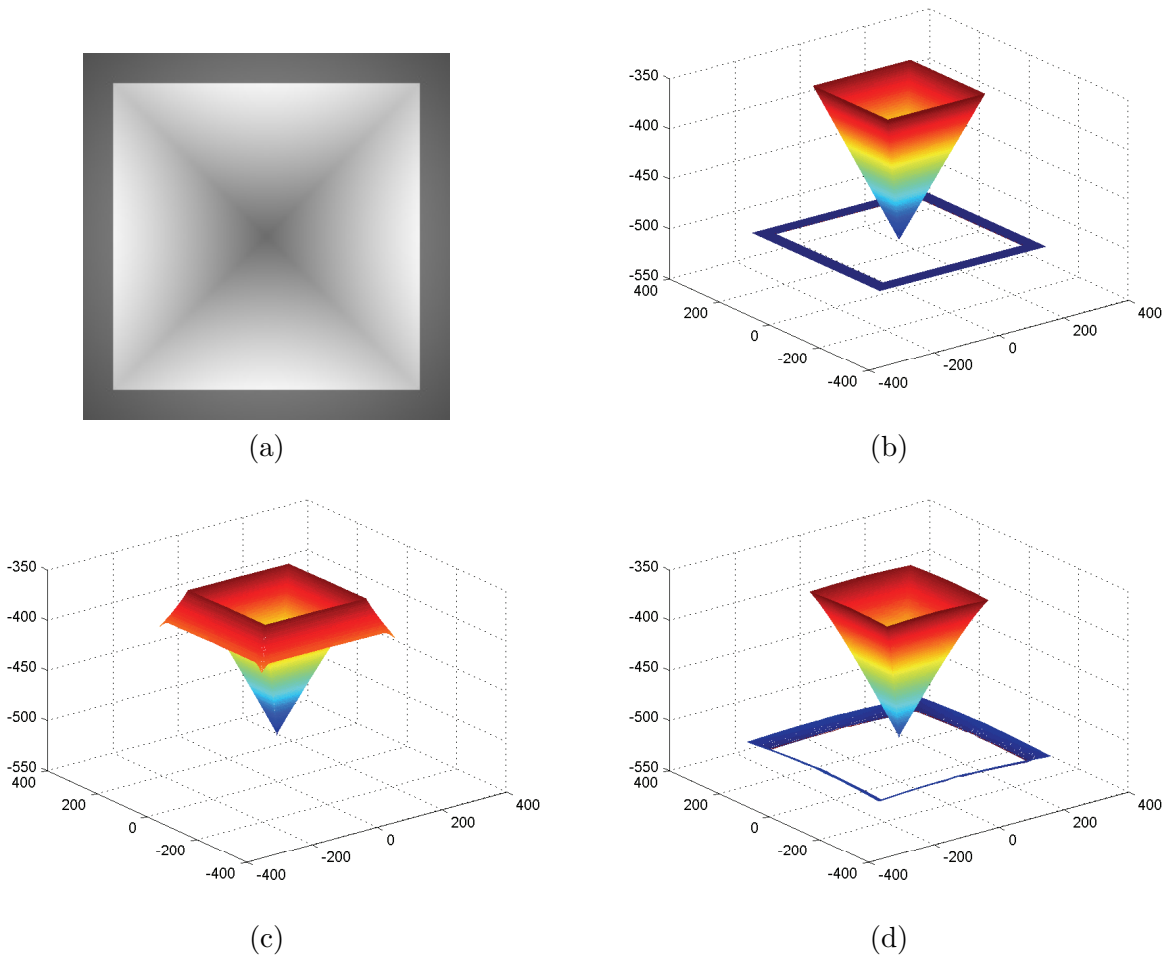

Figure 11. (a) *Input image,* (b) *input surface,* (c) *reconstructed surface by a direct application of the PSFS scheme (state constraint boundary conditions),* (d) *reconstructed surface after segmentation (state constraint boundary conditions).*

However, we note that, coherently with the previous results about ambiguity in the PSFS model, we cannot guarantee that inside each subdomain the reconstructed surface is the expected one.

Synthetic input data. We test the new algorithm on a synthetic photograph of an upside-down pyramid over a flat surface. See Figures 11(a) and 11(b) for the input photograph and the true surface (note that the pyramid hides most of the background).

Applying the PSFS algorithm directly, we obtain the surface depicted in Figure 11(c), where the discontinuity is totally lost. Note that the reconstructed surface has the same brightness function as the original one. Applying the PSFS algorithm after the segmentation, we have to solve two separate problems (for the pyramid and for the frame). The result is shown in Figure 11(d). This time the background is reconstructed at the right distance; i.e., the discontinuity is preserved. Nevertheless, the sides of the pyramid and the frame are not

Table 1
Errors for the test described in Figure 11.

Algorithm	L^1 error	L^∞ error
Direct	8.74%	26.71%
Presegmented	2.55%	4.80%

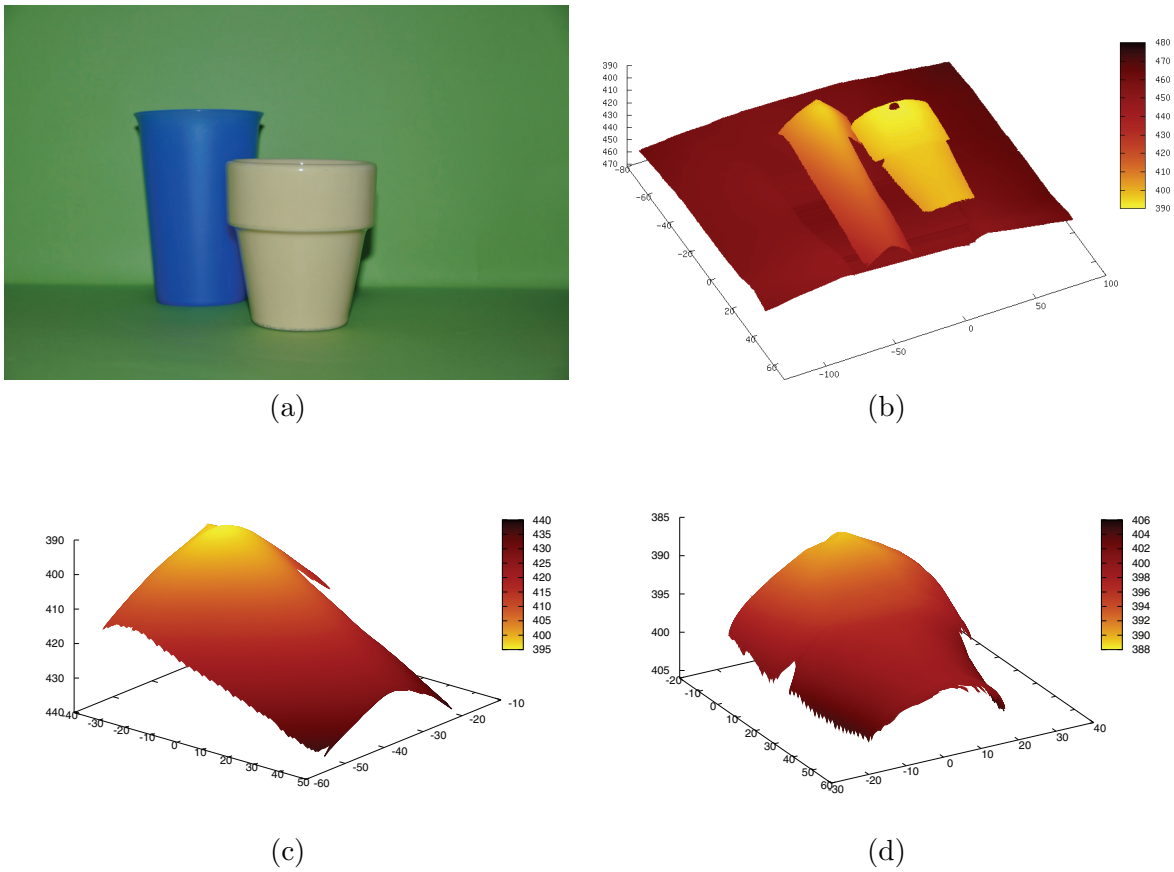

(a) (b) (c) (d)

Figure 12. (a) *Real-world input image and* (b) *its* 3-*D reconstruction.* (c) *Separate visualization of the mug segment reconstruction and* (d) *separate visualization of the cup segment reconstruction.*

completely flat as they should be. This is due to the fact that state constraint boundary conditions are not suitable here, because the local minimum points are on the boundary of the domain, as in Figure 6(c). For the experiment, we used a 256×256 grid and $\mathsf{f} = 250$. The reconstruction errors (depth error compared to the ground truth) are summarized in Table 1.

Real-world input data. As an example of a real-world image we consider the scene in Figure 12(a). The image was acquired with a Nikon D90 camera, and it has been downsampled to 800×531 pixels. The light source was the built-in camera flash. The focal length in multiples of the resulting pixel size is 1525. As is usual for real-world images, the reflectance and lighting parameters need to be estimated. We employed the following values for σ: 100000 for the background, 73000 for the blue mug, and 110000 for the beige cup.

The segment borders separating the cup from the mug as well as those separating the cup/mug from the background were obtained here by hand. They were enhanced a bit in order to mask out points where interreflections between the objects were very strong. The specular highlight at the upper lip of the cup was also masked out since such specular reflections are not included in the PSFS model. At the three resulting segments (subdomains)—cup, mug, and background—the PSFS equation was applied separately employing state constraint boundary conditions.

Let us turn to the corresponding experimental result; see Figure 12(b). The general shape of the objects and the background is captured in a rather accurate way. As expected, there is no tendency to enforce continuous transition between objects. This shows that the proposed idea of using state constraint boundary conditions at the borders of segmented objects works properly. Note that in the visualization of the whole scene together, the mug seems to have a wedge-like shape. This effect can be explained by specular highlights on the mug, which is not handled in the PSFS model. In this visualization, however, the effect looks more drastic than it actually is. To give a better impression on the shapes of the reconstruction, we also included separate visualizations of the mug and cup in Figures 12(c) and 12(d). The effect of the surface being pulled towards the optical center at specular highlights can also be observed in the reconstruction of the cup.

Concerning the quality of results, we observe some artifacts, as expected for this relatively difficult real-world input image. The cup is reflected on the surface of the mug, and, in addition, there are a lot of specular reflections as by the rough surface of the mug, so that its reconstruction is drawn towards the camera. Both cup and mug are reflected on the green cardboard of the background, so that the latter is not reconstructed perfectly flat. We also chose not to display the reconstruction of the ground on which the cup/mug are standing, since the absence of critical points there leads to a misinterpretation of the depth (as in the synthetic input data test, local minimum points are on the boundary of the domain). Moreover, the quality of the reconstruction of the ground is degraded since the reflections of both the cup and the mug are strongly visible there.

Conclusion. In this paper, we have studied analytically and numerically the PSFS model and the related Hamilton–Jacobi equation.

It turns out that ambiguities can still arise in the model as well as in practical computations. If any knowledge of the true depth is available, it is impossible to reconstruct surfaces such that

- they are not continuous (unless a presegmentation step is performed);
- local minima are located at points of nondifferentiability;
- local minima are located at the boundary.

We have also proved the convergence of a finite-difference scheme and a semi-Lagrangian scheme for the PSFS equation. In the latter case we employed an innovative technique for the proof that can also be useful in contexts other than PSFS. Our theoretical results on the numerics complement the analytical investigation of the ambiguity, ensuring that the ambiguity issues are not due to numerical artifacts: ambiguities arise systematically even if the scheme in use converges to the viscosity solution of the equation.

Modern models like the PSFS studied here have a significant potential for applications.

We believe that this paper represents an important step towards a deeper understanding of PSFS and other state-of-the-art SFS models, as well as towards the use of mathematically established numerical techniques in computer vision.

Appendix A. Derivation of PSFS equation in Cartesian coordinates. Starting from (2.1) and (2.2), we have (see Figure 1)

$$M(x,y) = \frac{\mathsf{f}u(x,y)}{d(x,y)} \begin{pmatrix} x \\ y \\ -\mathsf{f} \end{pmatrix},$$

where

$$d(x,y) = \sqrt{x^2 + y^2 + \mathsf{f}^2}.$$

The two vectors $\partial_x M$ and $\partial_y M$ form a basis in the plane orthogonal to the normal direction $\widehat{n}(x,y)$ at the point $M = M(x,y)$. We have

$$\partial_x M = \frac{\mathsf{f}}{d^3}\left(d^2u + d^2xu - x^2u, y(d^2u_x - xu), \mathsf{f}(-d^2u_x + xu)\right)^\top,$$
$$\partial_y M = \frac{\mathsf{f}}{d^3}\left(x(d^2u_y - yu), d^2u + d^2yu_y - y^2u, \mathsf{f}(-d^2u_y + yu)\right)^\top.$$

After some algebra, we find

$$\partial_x M \times \partial_y M = \frac{\mathsf{f}^2 u}{d^2}\left(\mathsf{f}\left(u_x - \frac{xu}{d^2}\right), \mathsf{f}\left(u_y - \frac{yu}{d^2}\right), \frac{\mathsf{f}^2 u}{d^2} + xu_x + yu_y\right)^\top,$$

which, after a normalization, gives

$$\widehat{n}(x,y) = \frac{\pm 1}{\sqrt{\mathsf{f}^2\|\nabla u\|^2 + (\nabla u \cdot (x,y))^2 + (\mathsf{f}u/d)^2}} \begin{pmatrix} \mathsf{f}(u_x - xu/d^2) \\ \mathsf{f}(u_y - yu/d^2) \\ \dfrac{\mathsf{f}^2 u}{d^2} + \nabla u \cdot (x,y) \end{pmatrix}. \tag{A.1}$$

Knowing that in each visible point M the normal $\widehat{n}$ points towards C, it follows that the correct sign in (A.1) is $+$, so we get from (A.1) and (2.4)

$$\omega(x,y) \cdot \widehat{n}(x,y) = \frac{\mathsf{f}u}{d\sqrt{\mathsf{f}^2\|\nabla u\|^2 + (\nabla u \cdot (x,y))^2 + (\mathsf{f}u/d)^2}}.$$

In conclusion, knowing that $r = \mathsf{f}\,u$, (2.6) can be written as

$$d\mathsf{f}u\sqrt{\mathsf{f}^2\|\nabla u\|^2 + (\nabla u \cdot (x,y))^2 + (\mathsf{f}u/d)^2} = \frac{1}{I}$$

or, using the change in the unknown $v = \ln(u)$, as

$$Id\mathsf{f}\sqrt{\mathsf{f}^2\|\nabla v\|^2 + (\nabla v \cdot (x,y))^2 + (\mathsf{f}/d)^2} = e^{-2v}, \tag{A.2}$$

which easily gives the Hamilton–Jacobi equation (2.7), since $Q = \mathsf{f}/d$.

Appendix B. Derivation of PSFS equation in spherical coordinates. Starting from (3.2)–(3.3), we have (see Figure 1)

$$u_r := \frac{M(\theta,\phi)}{r(\theta,\phi)} = \begin{pmatrix} \sin\theta\cos\phi \\ \sin\theta\sin\phi \\ \cos\theta \end{pmatrix}, \qquad u_\theta := \frac{\partial_\theta u_r}{\|\partial_\theta u_r\|} = \begin{pmatrix} \cos\theta\cos\phi \\ \cos\theta\sin\phi \\ -\sin\theta \end{pmatrix},$$

and

$$u_\phi := \frac{\partial_\phi u_r}{\|\partial_\phi u_r\|} = \begin{pmatrix} -\sin\phi \\ \cos\phi \\ 0 \end{pmatrix}.$$

The new system $\mathcal{S} = (u_r, u_\theta, u_\phi)$ is mobile and depends on the surface point M. The coordinates of M in this new system are $(r,0,0)^\top_{\mathcal{S}}$.

The two vectors $\partial_\theta M$ and $\partial_\phi M$ form a basis in the plane orthogonal to the normal direction $\widehat{n}(\theta,\phi)$ at the point $M = M(\theta,\phi)$. Since $M = ru_r$, we have

$$\partial_\theta M = r_\theta u_r + r u_\theta \quad \text{and} \quad \partial_\phi M = r_\phi u_r + r\sin\theta u_\phi,$$

and then

$$\partial_\theta M = (r_\theta, r, 0)^\top_{\mathcal{S}} \quad \text{and} \quad \partial_\phi M = (r_\phi, 0, r\sin\theta)^\top_{\mathcal{S}}.$$

We can write the coordinates of the normal vector in the new system $\mathcal{S}$ as

$$\widehat{n}(\theta,\phi) = \pm\frac{\partial_\theta M \times \partial_\phi M}{\|\partial_\theta M \times \partial_\phi M\|} = \pm\frac{(r\sin\theta, -r_\theta\sin\theta, -r_\phi)^\top_{\mathcal{S}}}{((r^2+{r_\theta}^2)\sin^2\theta + {r_\phi}^2)^{1/2}}. \tag{B.1}$$

Knowing that in each visible point M, the normal $\widehat{n}$ points towards C, and knowing that $\sin\theta \geq 0$, it follows that the correct sign in (B.1) is $-$, so we have

$$\omega(\theta,\phi)\cdot\widehat{n}(\theta,\phi) = (-1,0,0)^\top_{\mathcal{S}} \cdot \frac{(-r\sin\theta, r_\theta\sin\theta, r_\phi)^\top_{\mathcal{S}}}{((r^2+{r_\theta}^2)\sin^2\theta + {r_\phi}^2)^{1/2}}.$$

In conclusion, (3.1) can be written as

$$\frac{\sin\theta}{r((r^2+{r_\theta}^2)\sin^2\theta + {r_\phi}^2)^{1/2}} = I$$

or, in an equivalent form, as (3.5).

REFERENCES

[1] G. Barles, *Solutions de viscosité des équations de Hamilton-Jacobi*, Math. Appl. (Berlin) 17, Springer, Paris, 1994.

[2] G. Barles and P. E. Souganidis, *Convergence of approximation schemes for fully nonlinear second order equations*, Asymptot. Anal., 4 (1991), pp. 271–283.

[3] I. Barnes and K. Zhang, *Instability of the Eikonal equation and shape from shading*, M2AN Math. Model. Numer. Anal., 34 (2000), pp. 127–138.

[4] A. Blake, A. Zisserman, and G. Knowles, *Surface descriptions from stereo and shading*, Image Vision Comput., 3 (1985), pp. 183–191.

[5] M. Breuß, *The implicit upwind method for 1-D scalar conservation laws with continuous fluxes*, SIAM J. Numer. Anal., 43 (2005), pp. 970–986.

[6] M. Breuss, E. Cristiani, J.-D. Durou, M. Falcone, and O. Vogel, *Numerical algorithms for perspective shape from shading*, Kybernetika (Prague), 46 (2010), pp. 207–225.

[7] M. J. Brooks, W. Chojnacki, and R. Kozera, *Circularly symmetric Eikonal equations and non-uniqueness in computer vision*, J. Math. Anal. Appl., 165 (1992), pp. 192–215.

[8] A. R. Bruss, *The Eikonal equation: Some results applicable to computer vision*, J. Math. Phys., 23 (1982), pp. 890–896.

[9] F. Camilli and L. Grüne, *Numerical approximation of the maximal solutions for a class of degenerate Hamilton-Jacobi equations*, SIAM J. Numer. Anal., 38 (2000), pp. 1540–1560.

[10] F. Camilli and E. Prados, *Viscosity solution*, in Encyclopedia of Computer Vision, K. Ikeuchi, ed., Springer, to appear.

[11] F. Courteille, A. Crouzil, J.-D. Durou, and P. Gurdjos, *Towards shape from shading under realistic photographic conditions*, in Proceedings of the 17th International Conference on Pattern Recognition, Vol. II, Cambridge, UK, 2004, pp. 277–280.

[12] F. Courteille, A. Crouzil, J.-D. Durou, and P. Gurdjos, *Shape from shading for the digitization of curved documents*, Mach. Vision Appl., 18 (2007), pp. 301–316.

[13] E. Cristiani, *Fast Marching and Semi-Lagrangian Methods for Hamilton-Jacobi Equations with Applications*, Ph.D. thesis, Dipartimento di Metodi e Modelli Matematici per le Scienze Applicate, SAPIENZA Università di Roma, Rome, Italy, 2007.

[14] E. Cristiani, M. Falcone, and A. Seghini, *Some remarks on perspective shape-from-shading models*, in Proceedings of the 1st International Conference on Scale Space and Variational Methods in Computer Vision (Ischia, Italy, 2007), F. Sgallari, A. Murli, and N. Paragios, eds., Lecture Notes in Comput. Sci. 4485, Springer-Verlag, Berlin, Heidelberg, 2007, pp. 276–287.

[15] P. Dupuis and J. Oliensis, *An optimal control formulation and related numerical methods for a problem in shape reconstruction*, Ann. Appl. Probab., 4 (1994), pp. 287–346.

[16] J.-D. Durou, M. Falcone, and M. Sagona, *Numerical methods for shape-from-shading: A new survey with benchmarks*, Comput. Vis. Image Underst., 109 (2008), pp. 22–43.

[17] J.-D. Durou and D. Piau, *Ambiguous shape from shading with critical points*, J. Math. Imaging Vision, 12 (2000), pp. 99–108.

[18] M. Falcone and R. Ferretti, *Semi-Lagrangian Approximation Schemes for Linear and Hamilton–Jacobi Equations*, SIAM, Philadelphia, to appear.

[19] M. Falcone and M. Sagona, *An algorithm for the global solution of the shape-from-shading model*, in Image Analysis and Processing, Lecture Notes in Comput. Sci. 1310, Springer, Berlin, Heidelberg, 1997, pp. 596–603.

[20] B. K. P. Horn, *Obtaining shape from shading information*, in The Psychology of Computer Vision, P. H. Winston, ed., McGraw-Hill, New York, 1975, pp. 115–155.

[21] B. K. P. Horn, *Robot Vision*, MIT Press, Cambridge, MA, 1986.

[22] B. K. P. Horn and M. J. Brooks, eds., *Shape from Shading*, MIT Press Ser. Artificial Intelligence, MIT Press, Cambridge, MA, 1989.

[23] R. Kimmel, K. Siddiqi, B. B. Kimia, and A. Bruckstein, *Shape from shading: Level set propagation and viscosity solutions*, Int. J. Comput. Vision, 16 (1995), pp. 107–133.

[24] P.-L. Lions, E. Rouy, and A. Tourin, *Shape-from-shading, viscosity solutions and edges*, Numer. Math., 64 (1993), pp. 323–353.

[25] T. Okatani and K. Deguchi, *Shape reconstruction from an endoscope image by shape from shading technique for a point light source at the projection center*, Comput. Vis. Image Underst., 66 (1997), pp. 119–131.

[26] J. Oliensis, *Uniqueness in shape from shading*, Int. J. Comput. Vision, 6 (1991), pp. 75–104.

[27] E. Prados, F. Camilli, and O. Faugeras, *A unifying and rigorous shape from shading method adapted to realistic data and applications*, J. Math. Imaging Vision, 25 (2006), pp. 307–328.

[28] E. Prados, F. Camilli, and O. Faugeras, *A viscosity solution method for shape-from-shading without image boundary data*, M2AN Math. Model. Numer. Anal., 40 (2006), pp. 393–412.

[29] E. Prados and O. Faugeras, *"Perspective shape from shading" and viscosity solutions*, in Proceedings of the Ninth IEEE International Conference on Computer Vision, Vol. 2, Nice, France, 2003, pp. 826–831.

[30] E. Prados and O. Faugeras, *A generic and provably convergent shape-from-shading method for orthographic and pinhole cameras*, Int. J. Comput. Vision, 65 (2005), pp. 97–125.

[31] E. Prados and O. Faugeras, *Shape from shading: A well-posed problem?*, in Proceedings of the IEEE Computer Society Conference on Computer Vision and Pattern Recognition, Vol. 2, San Diego, CA, 2005, pp. 870–877.

[32] E. Prados, O. Faugeras, and F. Camilli, *Shape from Shading: A Well-Posed Problem?*, Rapport de Recherche RR-5297, INRIA Sophia Antipolis, Sophia Antipolis, France, 2004.

[33] E. Rouy and A. Tourin, *A viscosity solutions approach to shape-from-shading*, SIAM J. Numer. Anal., 29 (1992), pp. 867–884.

[34] A. Tankus, N. Sochen, and Y. Yeshurun, *A new perspective [on] shape-from-shading*, in Proceedings of the Ninth IEEE International Conference on Computer Vision, Vol. 2, Nice, France, 2003, pp. 862–869.

[35] A. Tankus, N. Sochen, and Y. Yeshurun, *Perspective shape-from-shading by fast marching*, in Proceedings of the 2004 IEEE Computer Society Conference on Computer Vision and Pattern Recognition, Vol. 1, Washington, DC, 2004, pp. 43–49.

[36] O. Vogel, M. Breuss, T. Leichtweis, and J. Weickert, *Fast shape from shading for Phong-type surfaces*, in Proceedings of the Second International Conference on Scale Space and Variational Methods in Computer Vision (Voss, Norway, 2009), X.-C. Tai, K. Mørken, M. Lysaker, and K.-A. Lie, eds., Lecture Notes in Comput. Sci. 5567, Springer-Verlag, Berlin, Heidelberg, pp. 733–744.

[37] O. Vogel, M. Breuss, and J. Weickert, *A direct numerical approach to perspective shape-from-shading*, in Proceedings of the Vision, Modeling, and Visualization Conference 2007, VMW 2007, H. Lensch, B. Rosenhahn, H.-P. Seidel, P. Slusallek, and J. Weickert, eds., Saarbrücken, Germany, AKA, Berlin, 2007, pp. 91–100.

[38] R. Zhang, P.-S. Tsai, J. E. Cryer, and M. Shah, *Shape from shading: A survey*, IEEE Trans. Pattern Anal. Mach. Intell., 21 (1999), pp. 690–706.